



NAVAL
POSTGRADUATE
SCHOOL

MONTEREY, CALIFORNIA

THESIS

**TESTING AND PERFORMANCE CHARACTERIZATION
OF THE SPLIT-FIELD POLARIMETER IN THE 3-5 μ m
WAVEBAND**

by

Tung, Yan Foo

December 2003

Thesis Advisor:

Thesis Co-Advisor:

Alfred W. Cooper

Gamani Karunasiri

Approved for public release; distribution is unlimited.

THIS PAGE INTENTIONALLY LEFT BLANK

REPORT DOCUMENTATION PAGE			<i>Form Approved OMB No. 0704-0188</i>	
Public reporting burden for this collection of information is estimated to average 1 hour per response, including the time for reviewing instruction, searching existing data sources, gathering and maintaining the data needed, and completing and reviewing the collection of information. Send comments regarding this burden estimate or any other aspect of this collection of information, including suggestions for reducing this burden, to Washington headquarters Services, Directorate for Information Operations and Reports, 1215 Jefferson Davis Highway, Suite 1204, Arlington, VA 22202-4302, and to the Office of Management and Budget, Paperwork Reduction Project (0704-0188) Washington DC 20503.				
1. AGENCY USE ONLY (Leave blank)		2. REPORT DATE December 2003	3. REPORT TYPE AND DATES COVERED Master's Thesis	
4. TITLE AND SUBTITLE: Testing and performance characterization of the split field polarimeter in the 3-5 μ m waveband.			5. FUNDING NUMBERS	
6. AUTHOR(S)				
7. PERFORMING ORGANIZATION NAME(S) AND ADDRESS(ES) Naval Postgraduate School Monterey, CA 93943-5000			8. PERFORMING ORGANIZATION REPORT NUMBER	
9. SPONSORING /MONITORING AGENCY NAME(S) AND ADDRESS(ES) N/A			10. SPONSORING/MONITORING AGENCY REPORT NUMBER	
11. SUPPLEMENTARY NOTES The views expressed in this thesis are those of the author and do not reflect the official policy or position of the Department of Defense or the U.S. Government.				
12a. DISTRIBUTION / AVAILABILITY STATEMENT Approved for public release; distribution is unlimited.			12b. DISTRIBUTION CODE	
13. ABSTRACT (maximum 200 words) <p>The infrared (IR) radiation emitted or reflected in an off-normal direction from a smooth surface is partially polarized. This principle can be used for enhanced discrimination of targets from backgrounds in marine environment. It has been shown that (man-made) targets do not demonstrate a pronounced polarization effect when observed at near normal exitance whereas the sea background radiation has a significant degree of polarization in slant observation directions. The NPS split-field polarimeter was previously designed and constructed to provide simultaneous image pairs in a single frame, differing only in the direction of linear polarization. The system can operate in both long wavelength (8-12 μm) and the mid wavelength (3-5 μm) with interchangeable polarizing splitter plates. In this thesis, tests were conducted to visually compare the polarizing effect on objects in the 3-5 μm waveband using the polarimeter and with the external polarizer. The image recorded in the laboratory with the horizontal and vertical polarizations depicts a contrast enhancement differing with varied aspect of the target. With the successful demonstration of the polarimeter operability, the performance of the thermal imager operated with and without the polarimeter was characterized by measuring its Minimum Resolvable Temperature Difference (MRTD) as a function of different spatial frequency. The measured performance was then compared against the same thermal imager using an external polarizer. The measured MRTD curve is used to model the system detection and recognition range using the Johnson criteria.</p>				
14. SUBJECT TERMS Thermal Imaging, Polarization, Infrared Radiation, Split Field Polarimeter			15. NUMBER OF PAGES 101	
			16. PRICE CODE	
17. SECURITY CLASSIFICATION OF REPORT Unclassified	18. SECURITY CLASSIFICATION OF THIS PAGE Unclassified	19. SECURITY CLASSIFICATION OF ABSTRACT Unclassified	20. LIMITATION OF ABSTRACT UL	

NSN 7540-01-280-5500

Standard Form 298 (Rev. 2-89)
Prescribed by ANSI Std. Z39-18

THIS PAGE INTENTIONALLY LEFT BLANK

Approved for public release; distribution is unlimited.

**TESTING AND PERFORMANCE CHARACTERIZATION OF THE
SPLIT-FIELD POLARIMETER IN THE 3-5 μ m WAVEBAND**

Yan Foo Tung
Defence Science & Technology Agency, Singapore
B.Eng (Hons), University of Manchester Institute of Science and Technology,
1992

Submitted in partial fulfillment of the
requirements for the degree of

**MASTER OF SCIENCE IN
COMBAT SYSTEMS TECHNOLOGY**

from the

**NAVAL POSTGRADUATE SCHOOL
December 2003**

Author: Yan Foo Tung

Approved by: Alfred W. Cooper
Thesis Advisor

Gamani Karunasiri
Thesis Co-Advisor

James Luscombe
Chairman, Department of Physics

THIS PAGE INTENTIONALLY LEFT BLANK

ABSTRACT

The infrared (IR) radiation emitted or reflected in an off-normal direction from a smooth surface is partially polarized. This principle can be used for enhanced discrimination of targets from backgrounds in marine environment. It has been shown that (man-made) targets do not demonstrate a pronounced polarization effect when observed at near normal exitance whereas the sea background radiation has a significant degree of polarization in slant observation directions.

The NPS split-field polarimeter was previously designed and constructed to provide simultaneous image pairs in a single frame, differing only in the direction of linear polarization. The system can operate in both long wavelength (8-12 μm) and the mid wavelength (3-5 μm) with interchangeable polarizing splitter plates.

In this thesis, tests were conducted to visually compare the polarizing effect on objects in the 3-5 μm waveband using the polarimeter and with the external polarizer. The image recorded in the laboratory with the horizontal and vertical polarizations depicts a contrast enhancement differing with varied aspect of the target. With the successful demonstration of the polarimeter operability, the performance of the thermal imager operated with and without the polarimeter was characterized by measuring its Minimum Resolvable Temperature Difference (MRTD) as a function of different spatial frequency. The measured performance was then compared against the same thermal imager using an external polarizer. The measured MRTD curve is used to model the system detection and recognition range using the Johnson criteria.

THIS PAGE INTENTIONALLY LEFT BLANK

TABLE OF CONTENTS

I.	INTRODUCTION.....	1
A.	GENERAL.....	1
B.	PREVIOUS WORK DONE	2
C.	PROBLEMS WITH EXTERNAL POLARIZERS.....	4
	1. Registration Time Delay	4
	2. Narcissus Effect.....	4
II.	FUNDAMENTAL INFRARED THEORY	5
A.	ELECTROMAGNETIC SPECTRUM	5
B.	INFRARED DEFINITIONS AND UNITS.....	7
C.	LAWS OF THERMAL RADIATION.....	8
	1. Blackbody Radiation	8
	2. Planck's Law	10
	3. Wien Displacement and Stefan-Boltzmann Law	12
D.	POLARIZATION.....	13
	1. Polarization Physics.....	13
	a) Stokes Parameters.....	14
	b) Emission Polarization.....	15
	c) Reflection Polarization	19
	2. Polarization Filtering Techniques	20
E.	TARGET TO BACKGROUND CONTRAST.....	21
F.	SENSITIVITY AND RESOLUTION LIMITS.....	22
III.	SPLIT FIELD POLARIMETER.....	25
A.	FUNCTIONALITY OF THE SPLIT FIELD POLARIMETER.....	25
IV.	IMAGE ACQUISITION AND ANALYSIS	29
A.	EQUIPMENT SET UP	29
	1. The CINCINNATI Infrared Thermal Imager.....	31
	2. External IR Polarizer.....	32
	3. Frame Grabber	33
B.	IMAGE ANALYSIS.....	34
	1. Thermal Imaging Using External IR Polarizer	34
	2. Thermal Imaging Using Split-field Polarimeter	37
V.	MINIMUM RESOLVABLE TEMPERATURE DIFFERENCE.....	39
A.	LABORATORY SETUP	39
	1. Four Bar Target.....	41
B.	MRTD MEASUREMENTS.....	43
VI.	MRTD RESULTS AND ANALYSIS	47
A.	THERMAL IMAGER MRTD	47
B.	THERMAL IMAGER WITH EXTERNAL POLARIZER MRTD	49
C.	THERMAL IMAGER WITH SPLIT FIELD POLARIMETER	51

D.	MRTD MEASUREMENT ANALYSIS	53
E.	RANGE PREDICTION	57
1.	Johnson Criteria	57
2.	System Prediction	63
VII.	CONCLUSIONS.....	67
VIII	FUTURE WORK	69
	APPENDIX A.....	71
	LIST OF REFERENCES.....	83
	INITIAL DISTRIBUTION LIST	85

LIST OF FIGURES

Figure 2.1	The Electromagnetic spectrum. From Ref. [8].	6
Figure 2.2	Spectral radiant exitance of a blackbody at various temperatures From [Ref. 5].	9
Figure 2.3	Sea emissivity and percent polarization for $\lambda=1 \mu\text{m}$ [Ref. 12].	16
Figure 2.4	Measured polarized signature components in the 7.5-12 μm band for selected paint samples viewed at 45° from normal [Ref. 14].	18
Figure 2.5	MRT is bounded by the system's resolution and visual sensitivity limit. From [Ref. 6].	24
Figure 2.6.	Two systems with different MRTs. From [Ref. 6.]	24
Figure 3.2	A close-up view of the polarizer and the gold mirrors.	27
Figure 3.3	Ray trace of split-field radiation path.	28
Figure 4.1	The laboratory set up for image analysis. (a) Detail of target in location, (b) Equipment in place for polarization testing.	30
Figure 4.2	The Cincinnati IRRIS-256LN Thermal Imager.	31
Figure 4.3	General output of a typical wire grid polarizer.	32
Figure 4.5	The image of the target in the visual waveband.	34
Figure 4.6	The image of the target in the 3-5 μm waveband.	34
Figure 4.7	Image of the target filtered by a horizontal polarizer.	35
Figure 4.8	Image of the target filtered by a vertical polarizer.	35
Figure 4.9	Schematic of the horizontal and vertical components for both the top face and the side.	36
Figure 4.10	Image of the target viewed through the split-field polarimeter.	38
Figure 5.1	Laboratory setup for the measurement of MRTD	40
Figure 5.2	The back and front plates of the four bar target.	41
Figure 5.3	The front side of the four bar target	42
Figure 5.4	MRTD pattern.	42
Figure 5.6	Sequence of images from resolvable to not resolvable.	44
Figure 6.1	Thermal imager MRTD plot.	48
Figure 6.2	Thermal imager with external polarizer MRTD plot.	50
Figure 6.3	Thermal imager with split field polarimeter MRTD plot.	52
Figure 6.4	The MRTD plots of the three configurations.	53
Figure 6.5	Thermal imager with external polarizer.	54
Figure 6.6	Thermal imager with split field polarimeter.	55
Figure 6.7	Radiant emission from the reflecting mirrors.	56
Figure 6.8	Target transfer probability function curve.	60
Figure 6.9	Schematic diagram of the discrimination performance prediction methodology. From [Ref. 17].	62
Figure 6.10	The MRTD as a function of Range. MRTD is for detection ($N_{50}=1$) with critical dimension 15 m.	64
Figure 6.11	The Apparent Temperature Difference as a function of Range for a Temperature Difference at source of 10°C.	65

Figure 6.12	MRTD and Apparent TBTD as a function of Range for detection of a 15 m critical dimension target.....	66
-------------	--	----

LIST OF TABLES

Table 2.1	Radiometric Quantities. From [Ref. 8].	7
Table 2.2	Emissivity (ϵ) of Common Materials. From [Ref.16].....	11
Table 6.1	Measured MRTD data of thermal imager.	47
Table 6.3	Measured MRTD data of thermal imager viewing through the split-field polarimeter.....	51
Table 6.4	Number of cycles required across target's critical dimension for various discrimination tasks. From [Ref. 17].....	58

THIS PAGE INTENTIONALLY LEFT BLANK

ACKNOWLEDGMENTS

I wish to express my gratitude to those who contributed to the successful completion of this thesis. Firstly, I would like to thank my sponsor DSTA, Singapore for giving me this opportunity to pursue my Masters degree in Naval Postgraduate School. Thanks to Mr. Sam Barone for his constant support in the laboratory. He is resourceful and very innovative when ever I needed logistic support in performing the experiment. Thanks to Professor Gamani Karunasiri for his guidance and help long before he is my second advisor. I would like to thank Professor Alfred W. Cooper for allowing me the opportunity to perform this thesis and providing his expert guidance and sharing his past experience. I will be grateful for the time we spent working together.

Finally, I wish to express my deepest gratitude to my wife. Her constant support, encouragement and understanding have made this goal possible.

THIS PAGE INTENTIONALLY LEFT BLANK

I. INTRODUCTION

A. GENERAL

Infrared systems have become a crucial part of vital military equipment. Due to its remote and passive nature, thermal imager has been used for weapons targeting, and detection of offensive military opponents and their weapons. With the large number of potential applications, intensive scientific and technological efforts have been made to improve the performance of these systems, particularly in improving contrast between the target and its background.

When the temperatures of a target and its background are nearly the same, detection becomes very difficult. It is possible to maximize the radiation contrast by a proper choice of eliminating radiation that interferes with or competes with the target radiation. In most cases, a target and its surrounding environment exhibit similar polarization characteristics. In the case of the target observed against a sea surface at near grazing incidence, we can eliminate a large percentage of the radiation from the sea surface than from the target by using a polarizer, thus increasing the contrast between the target and the background.

Large, high quality, efficient, infrared polarizers have only become available in recent years and so there have been quite a number of attempts to develop image improving techniques through the use of polarizers.

The NPS split-field polarimeter was previously designed and constructed to provide simultaneous image pairs in a single frame, differing only in the direction of linear polarization. The system can operate in both long wavelength (8-12 μm) and the mid wavelength (3-5 μm) with interchangeable polarizing splitter plates. Since the development of the polarimeter, it was calibrated for the

AGA-780 8-12 μm scanning thermal imager. Tests had since then been conducted in the 8-12 μm band.

In this thesis the 8-12 μm polarizing splitter was replaced with a 3-5 μm waveband polarizing splitter and the system adapted to the Cincinnati 3-5 μm thermal imager. Operability of the system was then tested by comparison of the polarizing effect using the polarimeter and with an external polarizer. The image recorded in the laboratory with the horizontal and vertical polarizations depicts a different contrast enhancement for the different aspects of the target. Both the polarimeter and the external polarizer exhibit identical characteristics of the polarized image. With the successful demonstration of the polarimeter operability, the performance of the thermal imager operating with and without the polarimeter was characterized by measuring its Minimum Resolvable Temperature Difference (MRTD) at varied spatial frequency. The measured performance is then compared against the same thermal imager using an external polarizer. The measured MRTD curve is used to model the system detection and recognition range using the Johnson criteria.

B. PREVIOUS WORK DONE

Early measurements of the effects of polarization on infrared radiation have generally used a single detector for consistency and inserted an external polarizer into the path of the radiation. The same field of view and target are examined both polarized and unpolarized with varied polarizer orientation.

The first NPS experiments using this configuration were conducted at the Monterey Bay Aquarium Research Institute Marine Operations Center located in Moss Landing CA. These experiments show that the infrared radiance from the sea surface at near grazing angle appears predominantly perpendicularly polarized (relative to the horizon) in regions of sun glint and parallel polarized otherwise [Ref. 1, 2, 3].

Tests conducted in Dutch coastal waters from Katwijk Beach Station for the Marine Aerosol Properties and Thermal Imager Performance Trial (MAPTIP) show improved target to background contrast with the polarizer horizontal, particularly at shallow angles of incidence from the sea surface. The same experiments show that the infrared radiance from the target and atmospheric background are generally unpolarized.

Experiments conducted during the Electro Optics Propagation Assessment in the Coastal Environment (EOPACE) multinational measurement series in San Diego in 1996 used the AGA-780 fitted with internal polarizers in filter wheels. The measurements confirmed that with the polarizers there is an improvement of target to background contrast. However, the internal polarizers, although easier to work with, still did not allow exact comparison of two images at the same time.

In the same project, the NPS constructed polarimeter was used to register the image in a 3.5×7 degree field of view in two orthogonal polarizations on two halves of the 7×7 degree field of view, thus allowing the exact comparison of two polarization images in a dynamic scenario.

C. PROBLEMS WITH EXTERNAL POLARIZERS

1. Registration Time Delay

There are several problems with the use of two orthogonally polarized images observed at different times for quantitative comparison. In order to make an accurate quantitative comparison between two images there must be pixel to pixel correspondence between the two images. In the case of either the internal or external polarizer installed, there is a time delay between the registration of the unpolarized image and the polarized image, thus a difference between the two images and an inherent error. This type of arrangement could only be useful if there is no movement of target against background and it is certain that the orientation of polarization of target and background is known. For a dynamic environment this is not possible.

2. Narcissus Effect

The narcissus effect is a condition sometimes observed with infrared imagers in that the image of the extremely cold detector cavity is focused back onto the image plane by reflection from an optical element and registered as a large black spot on the image. The black spot on the image results in an area of the field of view that can be examined qualitatively or quantitatively. This effect is quite noticeable in many of the original images taken by NPS using the external polarizing filter on the AGA-780. The narcissus effect can be minimized or eliminated by using polarizers internal to the body of the scanning imager but the time delay introduced by changing the polarization for the same field of view still exists. The internal polarizer is also in a fixed orientation, so polarization orientations are limited to the number of internal filters you can install in the imager. For sea targets only vertical and horizontal orientations may be required.

II. FUNDAMENTAL INFRARED THEORY

In order to follow a progressive approach to the objectives of this thesis a brief presentation of the basic laws and theories of Infrared technology is necessary. Theories necessary to comprehend the basic physical phenomena associated with this work will be addressed.

A. ELECTROMAGNETIC SPECTRUM

The propagation of electromagnetic energy can be described in terms of spatial and temporal variations in electric and magnetic fields. Typical examples of electromagnetic waves are light rays, radio waves, radar beams and infrared radiation. The optical radiation covers the electromagnetic spectrum from the Ultraviolet (UV) range throughout the visible and up to the Infrared (IR) portion of the spectrum. Figure 2.1 shows the regions of the spectrum.

The infrared portion of the spectrum lies between the visible (shorter wavelength) and the radio frequency (longer wavelength) regions. This region corresponds to the range of wavelengths from approximately 0.7 μm to 1000 μm . The near infrared (NIR) is characterized by wavelengths from 0.7 μm to 0.9 μm , and the short-wave infrared (SWIR) is characterized by wavelengths from 0.9 μm to 3.0 μm . Since the short-wave band radiance includes mostly reflected solar radiation it can be imaged with Image intensifier devices that collect and amplify the reflected light waves. The mid-wave (MWIR) is characterized by wavelength from 3.0 μm to 6.0 μm and the long-wave infrared (LWIR) characterized by wavelengths from 6.0 μm to 15.0 μm . The long-wave band is called the “thermal radiation region” because thermal emission is greater than the solar reflection in these wavelengths. Due to this characteristic of the mid-wave and long-wave bands, thermal imaging system such as Forward Looking Infrared (FLIR) Systems operate in these bands.

The factors such as the form of the radiation, methods of detection, and the atmospheric transmission mostly determine these sub-bands. The region

from 5 μm to 8 μm is also a part of the infrared spectrum, but it is not used due to the high absorptivity of the atmosphere in this area.

Infrared radiation complies with the laws of electromagnetism, as stated by Maxwell's Equations.

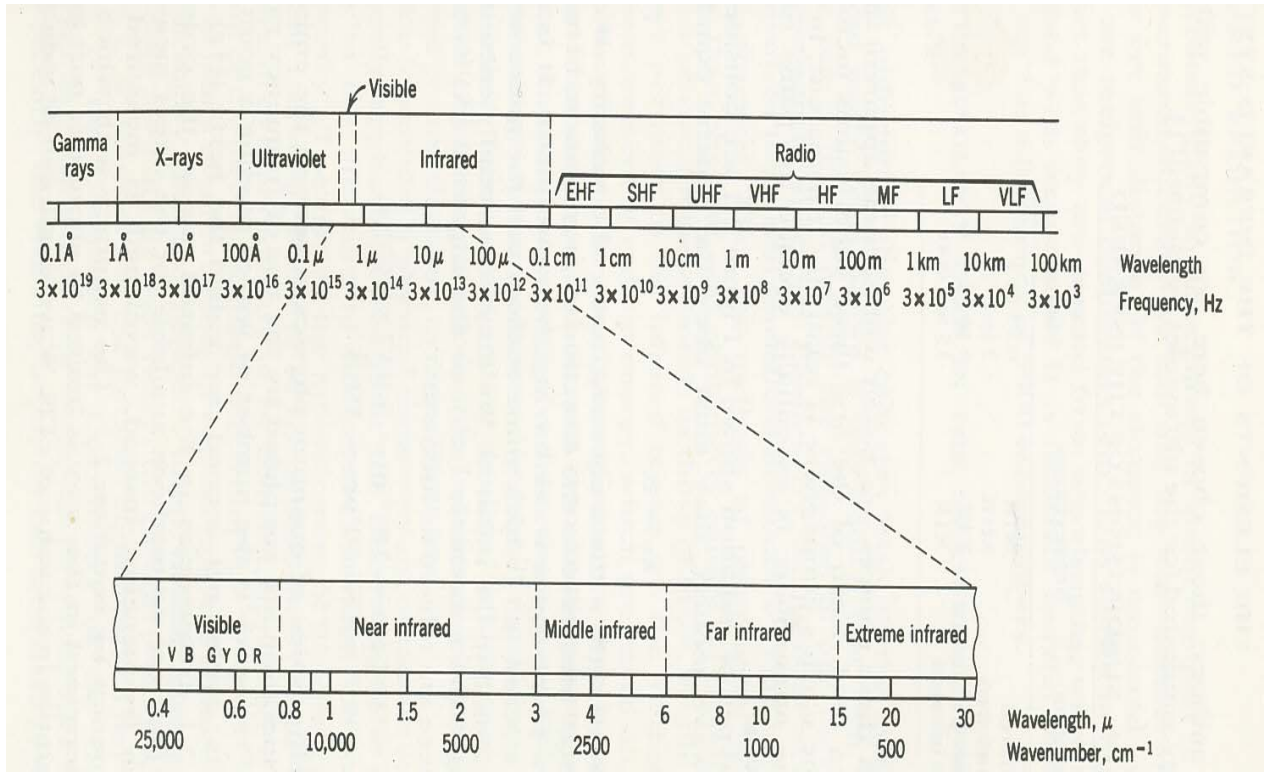


Figure 2.1 The Electromagnetic spectrum. From Ref. [8].

B. INFRARED DEFINITIONS AND UNITS

Infrared science makes use of many specific definitions and uses varied units. Table 2.1 shows some fundamental radiometric quantities and units associated with infrared radiation. In this table:

- Radiant exitance (emittance) of flux density, M , is the radiant flux density leaving the target surface per unit area.
- Irradiance or radiant flux surface density, E , is the radiant power incident on a unit area of surface.
- Radiant intensity, I , is the radiant power exiting a point source along a given direction within a unit solid angle.
- Radiance, or radiant intensity surface density in a given direction, L , is the radiant power per unit solid angle per unit area leaving from or incident on an area projected perpendicular to the direction of radiant energy flow.
- In the table U represents radiant energy, S represents surface area, and Ω (sr) represents solid angle.

Symbol	Quantity	Units(metric)	Description
U	Radiant Energy	Joules	--
P	Radiant Power	Watts	$\partial U/\partial t$
M	Radiant Exitance	Watt/m^2	$\partial P/\partial S$
E	Radiant Incidence	Watt/m^2	$\partial P/\partial S$
I	Radiant Intensity	Watt/sr	$\partial P/\partial \Omega$
L	Radiance	$\text{Watt}/\text{m}^2 \text{ sr}$	$\partial^2 P/\partial S \partial \Omega$

Table 2.1 Radiometric Quantities. From [Ref. 8].

C. LAWS OF THERMAL RADIATION

1. Blackbody Radiation

When we consider the total optical power that is incident on an object, we can distinguish three distinct outcomes. Some fraction of this total radiant energy is absorbed, some is reflected and some is transmitted through the surface of the object. Therefore the ratios of each of these to the incident power must add up to unity. [Ref. 16]

$$\alpha + \rho + \tau = 1 \quad (2.1)$$

where:

$$\alpha_{\text{(absorptivity)}} = P_{\text{absorbed}} / P_{\text{incident}}$$

$$\rho_{\text{(reflectivity)}} = P_{\text{reflected}} / P_{\text{incident}}$$

$$\tau_{\text{(transmissivity)}} = P_{\text{transmitted}} / P_{\text{incident}}$$

An ideal blackbody can be defined as an ideal emitter and an ideal absorber i.e. absorptivity (α) = emissivity (ϵ) = 1. Thus the blackbody has reflectivity (ρ) and transmissivity (τ) both of zero. The blackbody radiator is an idealized source of radiant energy having defined properties. It is perfectly diffuse, radiates at all wavelengths, and at all temperatures its spectral radiant exitance is the maximum possible for any actual thermal source at the same temperature. The characteristics of many real sources of radiation approach the ideal quite closely; many others are conveniently described by corrections to the blackbody curve. [Ref. 5] The spectral radiant exitance of a blackbody is presented in Figure 2.2, as a function of wavelength and source temperature.

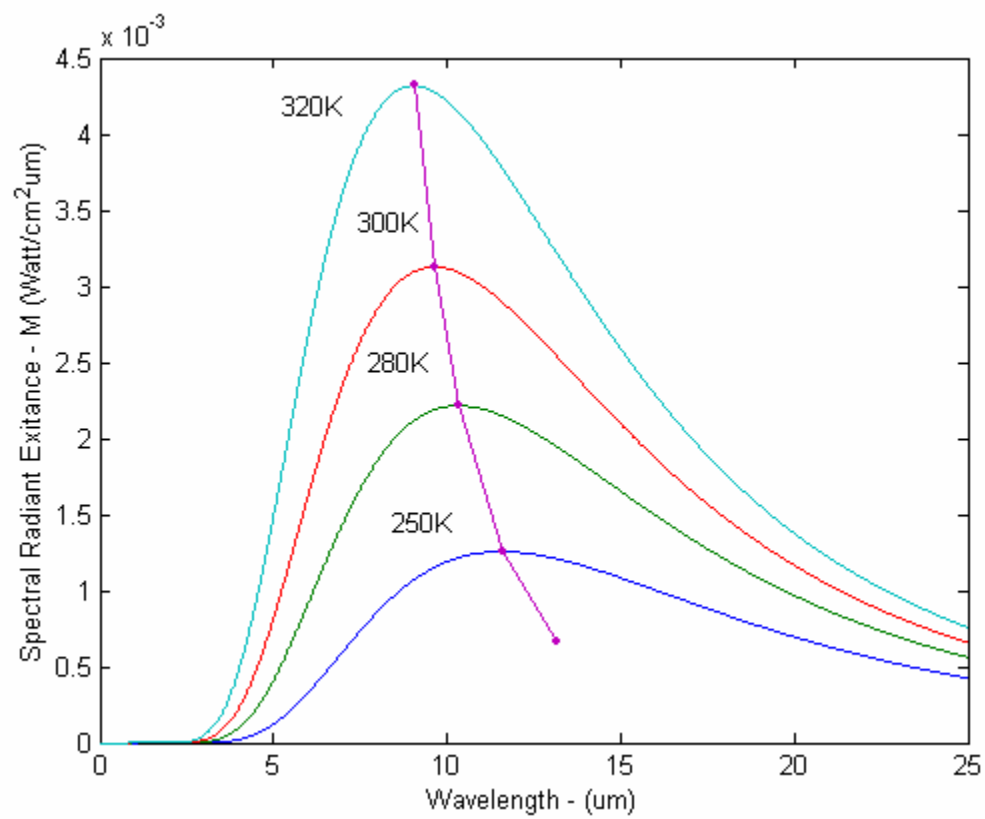


Figure 2.2 Spectral radiant exitance of a blackbody at various temperatures From [Ref. 5].

2. Planck's Law

The equation that represents a blackbody's spectral exitance as a function of its temperature is known as Planck's Radiation Law and has the following form:

$$M_{\lambda,b} = \frac{2\pi hc^2}{\lambda^5 (e^{hc/\lambda kT} - 1)} \quad (2.2)$$

where:

$M_{\lambda,b}$	=	The blackbody spectral radiant exitance at wavelength λ (Watt/cm ² μm)
c	=	The vacuum velocity of light (3×10^8 m/s)
h	=	Planck's constant (6.63×10^{-34} Joules/s)
k	=	Boltzmann's constant (1.38×10^{-23} Joule/K)
T	=	Absolute temperature of the blackbody (K)
λ	=	Wavelength (μm)

In infrared theory the radiant exitance is directly proportional to the emissivity. The "emissivity", ϵ , of a surface is the ratio of radiant exitance emitted from a surface to that emitted from a blackbody (perfect emitter) at the same temperature.

The radiant exitance of a non blackbody then can be defined as

$$M_{\lambda} = \epsilon_{\lambda} M_{\lambda,b} \quad (2.3)$$

where ϵ_{λ} is the spectral emissivity which is always less than 1 for non-blackbodies. [Ref. 5]

A material which has an emissivity that is independent of wavelength is called a gray body. Table 2.2 shows emissivities of some common materials.

Material	ϵ
Aluminum Foil	0.09
Copper, polished	0.05
Copper, oxidized	0.78
Carbon	0.95
Paint, oil	0.94
Concrete	0.92
Sand	0.90

Table 2.2 Emissivity (ϵ) of Common Materials. From [Ref.16].

To describe the radiant exitance from a gray body the Planck function must be multiplied by the emissivity of the surface.

3. Wien Displacement and Stefan-Boltzmann Law

Figure 2.2 shows blackbody curves in terms of the radiant exitance as a function of wavelength for a number of different temperatures, each one of higher temperature completely above the others. The wavelength of the peaks, i.e. the wavelengths where the maximum radiation occurs for a given temperature, can be found from the equation known as the Wien Displacement Law,

$$\lambda_{\max} = \frac{2898}{T} \quad (2.4)$$

where:

λ_{\max} = wavelength where the peaks of radiation occurs (μm).

The peak wavelength in micrometers is approximately 3000 divided by the temperature in Kelvin.

The Planck curve can be integrated to obtain the expression for total radiant exitance at all wavelengths.

$$W_b = \sigma T^4 \quad (2.5)$$

where:

W_b = Total radiant exitance of a blackbody

σ = The Stefan-Boltzmann constant (5.67×10^{-8} Watts/m²K⁴)

T = The temperature in K

For use with non-blackbody sources this is modified by the inclusion of an “effective emissivity”, ϵ , giving the form

$$W_b = \epsilon \sigma T^4 \quad (2.6)$$

This equation is known as the Stefan-Boltzmann Law.

D. POLARIZATION

1. Polarization Physics

The polarization of light is one of its fundamental properties, the others being its intensity, wavelength and coherence. Christian Huygens was the first to suggest that light was not a scalar quantity. This vector nature of light is called polarization. Light propagating in air or space is a transverse electromagnetic wave. Its electric field is perpendicular to the magnetic field and they both are mutually orthogonal to the propagation direction. In the case that the plane of vibration of the electric vector is spatially fixed, the wave is said to be linearly polarized. Under the conditions where the electrical vector rotates in such a way that an ellipse is created when viewed from the direction of propagation, then it is said to be elliptically polarized (with the special case of circular polarization being included in this general category). The fundamental laws and polarization equations describe the basic parameters of polarization of the sea and sky background as well as the target.

a) Stokes Parameters

Sir George Gabriel Stokes found that the polarization behavior could be completely represented in terms of four measurable quantities known as the Stokes polarization parameters. The Stokes polarization parameters for a plane wave are [Ref. 9]:

$$I = E_s^2 + E_p^2 \quad (2.7)$$

$$M = E_s^2 - E_p^2 \quad (2.8)$$

$$C = 2E_s E_p \cos \delta \quad (2.9)$$

$$S = 2E_s E_p \sin \delta \quad (2.10)$$

where:

I = the total intensity of the light

M = the intensity of linear polarized light either normal or parallel to the plane of incidence

E_s = the components of the wave electric field normal to the plane of incidence

E_p = the components of the wave electric field parallel to the plane of incidence

C = intensity of linear $\pm 45^\circ$ polarized light

S = the intensity of right or left circular polarization contained within the beam

δ = the phase difference between the s and p components of the E field.

The first parameter (I) expresses the total intensity of the optical field and the other three (M,C,S) describe the polarization state. Stokes parameters can be applied not only to completely polarized light but also to partially polarized light and unpolarized light. The degree of polarization is the ratio of the intensities of the polarized to the total intensity:

$$P = \frac{I_{\text{pol}}}{I_{\text{tot}}} = \frac{(M^2 + C^2 + S^2)^{\frac{1}{2}}}{I}, \quad 0 \leq P \leq 1 \quad (2.11)$$

where:

I_{pol} = the intensity of the sum of the polarization components

I_{tot} = the total intensity of the beam

The effects that result from polarization depend on the emission as well as the reflection properties of the various materials.

b) Emission Polarization

The thermal energy emitted by various targets and their background is inherently polarized. For sea targets the emission characteristics of the sea and the sky background are of great importance since a significant contrast improvement can be obtained by filtering off the background.

(1) Sea Emission Polarization. The mathematical models describing sea surface polarizations are complex and are analyzed in great detail in Reference 1 and 10. What is important for this work is the fact that both emitted and reflected components of the sea surface radiance will show polarization, predominantly in orthogonal directions. For most materials there is only a small range of angles at which elliptical polarization occurs. Even in those cases the phase difference between orthogonal components is small enough

(due to small dielectric constants) that an approximation of linearly polarized light at all angles is valid [Ref. 11].

In Figure 2.3 the polarization of emission for 1 μm wavelength and 14 m/sec wind speed is presented [Ref. 12]. The percentage of polarization Q is defined by:

$$Q = 100 \times \frac{\epsilon_{\parallel} - \epsilon_{\perp}}{\epsilon_{\parallel} + \epsilon_{\perp}} \quad (2.12)$$

where:

ϵ_{\parallel} = emissivity of each surface referred to the horizontal direction

ϵ_{\perp} = emissivity of each surface referred to the vertical direction

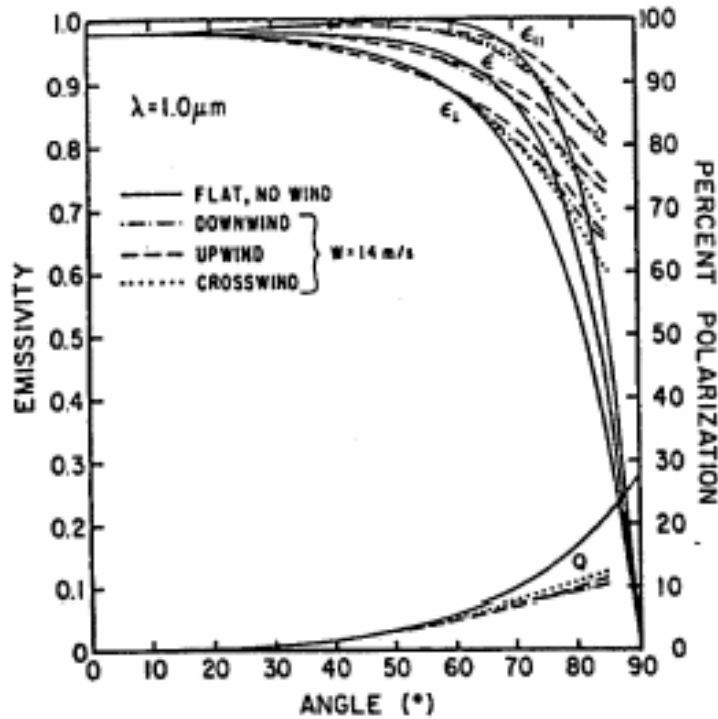


Figure 2.3 Sea emissivity and percent polarization for $\lambda=1 \mu\text{m}$ [Ref. 12].

The results from Figure 2.3 hold true for all wavelengths less than or equal to 10 μm , excluding the absorption bands [Ref. 11]. It should be noted that the maximum percentage of polarization is observed at angles near the grazing angle.

(2) Sky Emission Polarization. Infrared radiation emitted from the sky is unpolarized [Ref. 13]. As a result there will be no improvement in the contrast measurements when the sky is viewed directly. What should be mentioned however, is that when the sky is viewed towards the zenith its emission is less, due to the fact that the atmosphere contains water vapor and aerosols (absorbers) that act as good emitters but have small number densities. So the sky radiance increases along with the zenith angle towards the horizon to that of a blackbody with atmospheric temperature. This is due to the increasing thickness of the atmosphere encountered at these angles [Ref. 10].

(3) Target Emission Polarization. It has been demonstrated that painted surfaces such as those found on ships and other vehicles display emission polarization. In Figure 2.4 [Ref. 14] a series of various paint measurements is presented ranging from very smooth to sand paint mixtures.

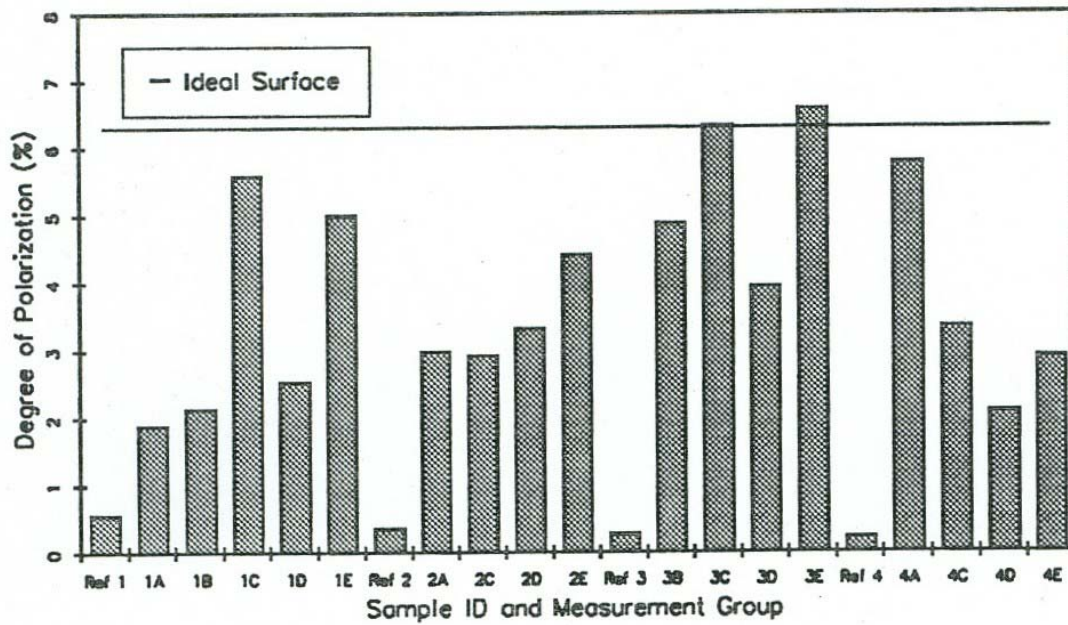


Figure 2.4 Measured polarized signature components in the 7.5-12 μ m band for selected paint samples viewed at 45° from normal [Ref. 14].

The line for an ideal surface denotes the degree of polarization that would be seen from a perfectly specular reflector. The rougher the sample the less is the degree of polarization. The degree of polarization depends also on the index of refraction of the paint and any possible degradation due to the roughness of the surface.

c) Reflection Polarization

From the total power law it follows that:

$$\alpha + \rho + \tau = 1 \quad (2.13)$$

where:

$$\alpha = \text{Absorptivity}$$

$$\rho = \text{Reflectivity}$$

$$\tau = \text{Transmissivity}$$

For a perfectly opaque body, $\tau = 0$ so:

$$\varepsilon + \rho = 1 \quad (2.14)$$

The emissivity was defined in Section 2.b.3. The reflectance ρ will be degraded by the absorption properties of the specific body.

(1) Sea Reflection Polarization. By applying the Fresnel equations to a Cox-Munk sea surface slope distribution the following equations are derived [Ref. 10].

$$\varepsilon_{\perp} = 1 - \rho_{\perp} \quad (2.15)$$

$$\varepsilon_{\parallel} = 1 - \rho_{\parallel} \quad (2.16)$$

$$\varepsilon = \frac{\varepsilon_{\perp} + \varepsilon_{\parallel}}{2} \quad (2.17)$$

$$\rho = \frac{\rho_{\perp} + \rho_{\parallel}}{2} \quad (2.18)$$

$$\varepsilon = 1 - \rho \quad (2.19)$$

The sea surface acts as an opaque body. The percentage polarization due to reflection is given by:

$$P=100\times\frac{\rho_{\perp}-\rho_{\parallel}}{\rho_{\perp}+\rho_{\parallel}} \quad (2.20)$$

(2) Sky Reflectance. The sky appears to be a poor reflector due to its very good absorption characteristics (because of the atmospheric water and aerosols).

(3) Target Reflectance. The total polarization coming from a thermal target will depend on the balance between thermal emission and reflection of incident radiance. The maximum results due to reflection polarization will occur nearer to grazing incident angles.

2. Polarization Filtering Techniques

The method of polarization filter construction has in the past been mainly by using anisotropic crystals or wire grids. The wire grid technique has been applied in recent years by using lithographic techniques. That is, a conducting grid is deposited on a transparent substrate. The grid spacing must be comparable to the wavelength.

In this way the filter will block incoming radiation with the electric field parallel to the orientation of the grid. That is because the wire grid induces currents that reflect the part of the incoming wave with electric field parallel to the wire grid. In order for this process to take place the spacing of the wires in the grid must be of the order of the wavelength of the incident radiation.

For the infrared region typical transparent substrates are materials such as Silicon and Germanium. These materials require anti-reflection coatings.

E. TARGET TO BACKGROUND CONTRAST

The basic parameter that is used by a system or an operator in order to distinguish between a target and its surroundings is the contrast. The contrast is the difference between the irradiance received from a target pixel and the irradiance received coming from the neighboring background.

There are several definitions and types of contrast used. What is known as inherent contrast [Ref. 6], or contrast relative to the background is defined by:

$$C_o = \frac{N_{\text{target}} - N_{\text{background}}}{N_{\text{background}}} \quad (2.21)$$

where:

N_{tgt} = irradiance coming from the target

$N_{\text{background}}$ = irradiance coming from the background

An alternative definition of contrast is presented by the following formula:

$$C_o = \frac{N_{\text{target}} - N_{\text{background}}}{N_{\text{target}} + N_{\text{background}}} \quad (2.22)$$

The absolute contrast is given by:

$$\Delta N = N_{\text{target}} - N_{\text{background}} \quad (2.23)$$

When comparing two images, it is useful to quantify the increase or decrease in image contrast improvement. So the improvement factor is defined as:

$$F = \frac{\Delta N_1}{\Delta N_2} \quad (2.24)$$

The contrast improvement factor for polarization over the unpolarized case is given by:

$$F_{\text{pol}} = \frac{C_{\text{pol}}}{C_{\text{unpol}}} \quad (2.25)$$

where:

C_{pol} = contrast of the image scene with polarizer

C_{unpol} = contrast of the image scene without polarizer

It has been shown that the target to background contrast outside the sun glint corridor can be improved with the use of horizontal polarization filters [Ref. 3].

F. SENSITIVITY AND RESOLUTION LIMITS

Image quality of a system is based on spatial resolution or sensitivity. Resolution has been in use so long that it is thought to be something fundamental that uniquely determines system performance. [Ref. 6]. It implies something about the smallest detail that can be perceived. Resolution does not include the effects of system noise. Resolution considerations provide a back-of-the-envelope approximation from which target range can be estimated.

$$\text{Range} = R = \frac{\text{target size}}{\text{resolution}} \quad (2.26)$$

Sensitivity deals with the smallest signal that can be detected. It is usually taken as that signal that produces a signal-to-noise ratio (SNR) of unity at the system output. Sensitivity is dependent upon the light-gathering properties of the

optical system independent of resolution. Sensitivity limitations provide another back-of-the envelope approximation. The SNR is

$$\text{SNR} = \frac{(\tau_{\text{atm-ave}})^R \Delta I}{\text{system noise}} \quad (2.27)$$

where:

ΔI = intensity difference between the target and its immediate background

$\tau_{\text{atm-ave}}$ = average atmosphere attenuation coefficient

R = Range

For infrared imaging systems, the target-background intensity difference is specified by a differential temperature (ΔT). The system noise is taken as the noise equivalent differential temperature (NEDT). This approximation only applies to those targets whose angular sub-tense is large compared to the system resolution at the calculated range.

Overall system response depends on both sensitivity and resolution. As shown in Figure 2-5, the minimum resolvable temperature (MRT) is bounded by sensitivity and resolution considerations. Different systems (Figure 2-6) may have different MRTs. System A has a better sensitivity. It has a lower MRT at low spatial frequencies. As mid-range spatial frequencies, the systems are approximately equivalent and it can be said they provide equivalent performance. System B has better resolution and can display finer detail than System A. Figure 2-6 illustrates that neither sensitivity resolution nor any other single parameter can be used to compare systems.

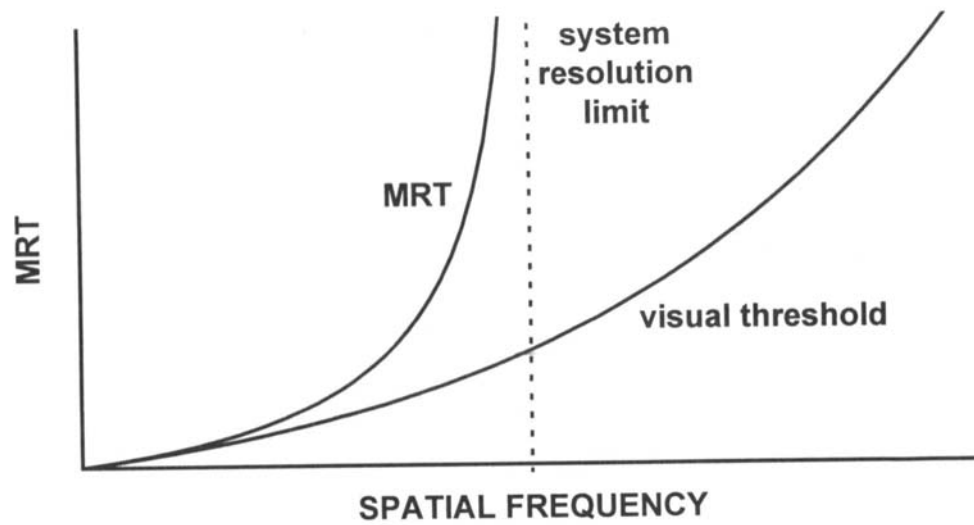


Figure 2.5 MRT is bounded by the system's resolution and visual sensitivity limit. From [Ref. 6].

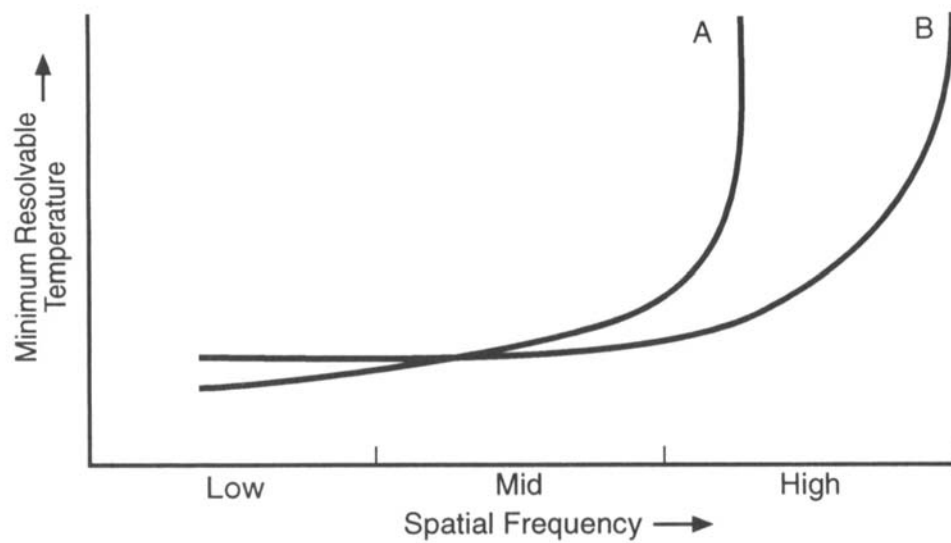


Figure 2.6. Two systems with different MRTs. From [Ref. 6].

III. SPLIT FIELD POLARIMETER

NPS Professors Cooper and Crittenden designed and constructed a device referred to as a split-field polarimeter. The split-field system approach possesses many advantages over external and internal filter placement normal to the path of the radiation, particularly in elimination of time lags and registration problems between orthogonal polarizations. The split-field polarimeter is based on the use of a wire grid polarizer as a beam splitter to separate the vertically and horizontally polarized radiation from the thermal imager field of view into two different optical paths and then reassemble the radiation into adjacent orthogonally polarized images. The general features of the split-field polarimeter are:

1. Simultaneous display and recording of orthogonally polarized images.
2. Utilization of entire field of view for display.
3. Adaptability to different imaging systems.
4. Dual-band (3-5 μm and 8-12 μm) operation using interchangeable filters.
5. F/1.87, 99 mm focal length optics.

The polarimeter was designed for operation with the AGA 780 scanning imager. In this work it was adapted to the Cincinnati staring imager.

A. FUNCTIONALITY OF THE SPLIT FIELD POLARIMETER

The optical elements are matched to the field of view of the AGA 780 thermal imager. The 7° lens was chosen due to the unavailability of polarizer of adequate size for the 3.5° lens as well as to minimize the complexity of the design. The split field optical path consists of two lenses, for collimating the

radiation, a wire grid polarizing splitter, and four mirrors to fold and redirect the radiation to the input lens of the thermal imager. Figures 3.1 and 3.2 show the split field optical elements from target to imager and Fig 3.3 shows the path of light rays through the split field optical elements.

The radiation from the target enters the polarimeter through the collimated lens at position A and strike the polarizing splitter at position F. The radiation striking the polarizing splitter at a 45° angle of incidence separates into perpendicular and horizontal components. The polarizing splitter reflects the vertically polarized light to mirror B, from which it is reflected again to pass through an intermediate image plane at I to the mirror D, from which it is directed through the second lens at position H.

The polarizing splitter transmits the horizontally polarized light to mirror E, from which it is reflected to pass through an adjacent portion of the intermediate image plane at I to the mirror D, from which it is directed through the second lens at position H. The light from the background temperature control plate, position G, strikes the polarizing splitter at position F where it follows the same paths as the light from the target. The two paths are partially obstructed by the set of reflecting mirrors so as to remove the unwanted portions of the field of view, defining a new limiting optical field aperture at the intermediate image plane. The top and bottom quarters of the field of view are removed from each channel, leaving only the central half of the image. The light passes through the intermediate image plane where the two $3.5^\circ \times 7^\circ$ orthogonally polarized images are combined into one $7^\circ \times 7^\circ$ image, which is then displayed by the thermal imager.

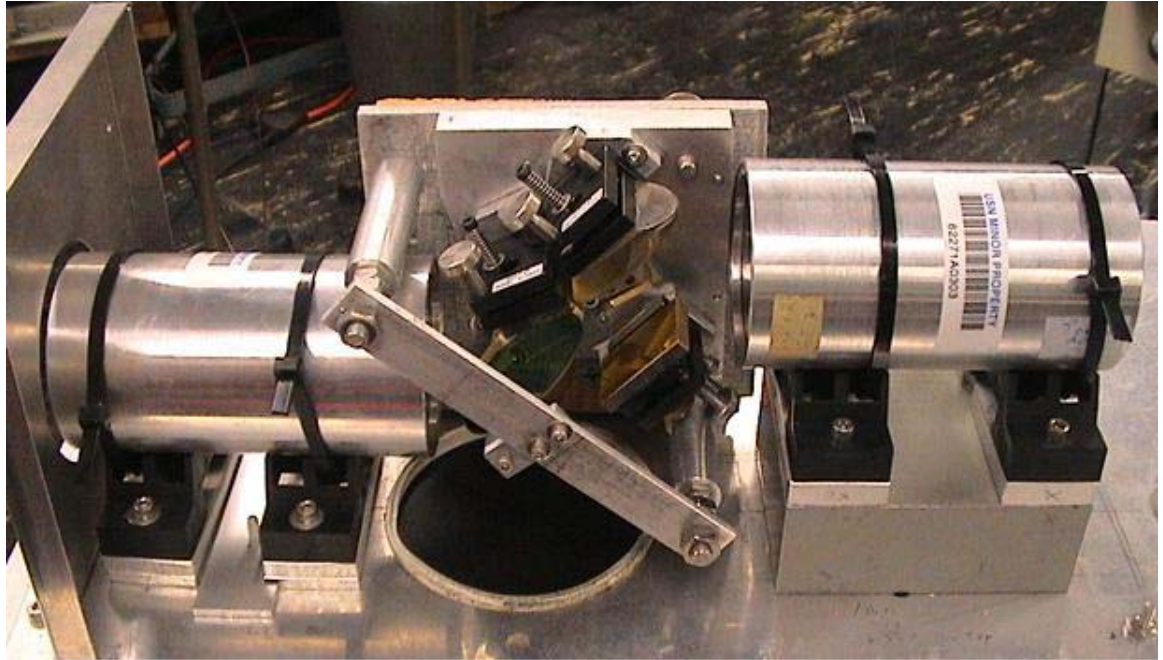


Figure 3.1 Split field optics equipment.

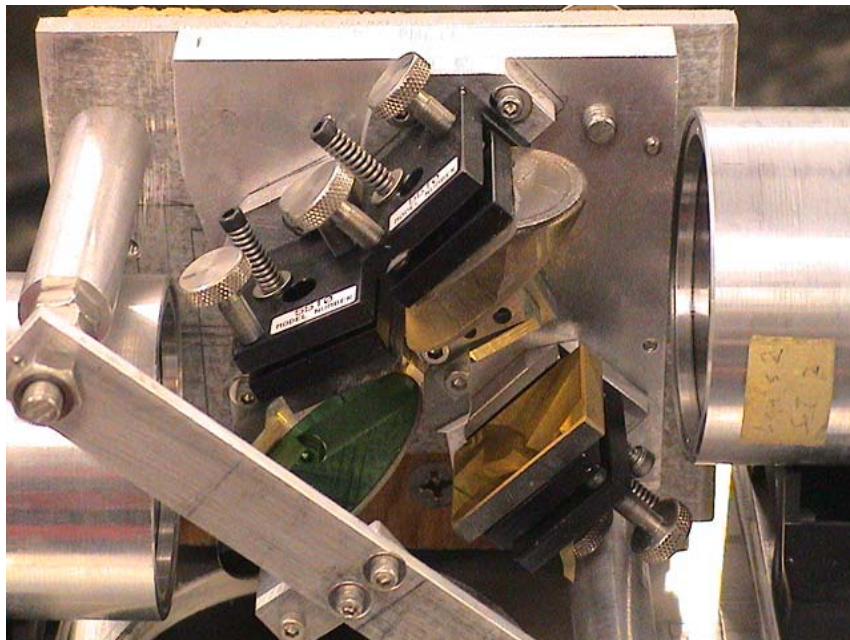
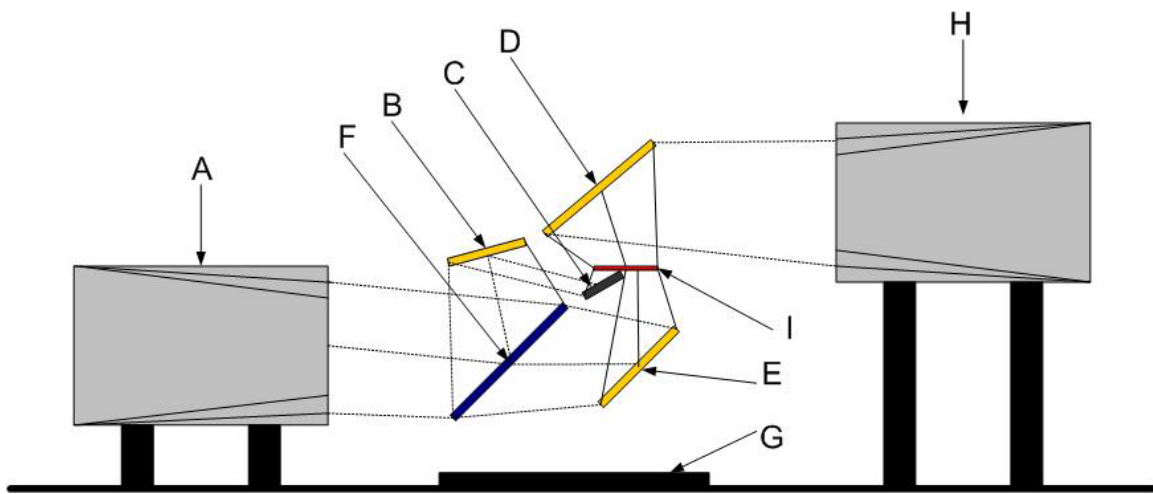


Figure 3.2 A close-up view of the polarizer and the gold mirrors.



A – Lens 1

H – Lens 2

B,C,D,E – Reflecting Mirrors

F – Polarizing Splitter

G – Background Temperature Control Plate

I – Intermediate Image Plane

Figure 3.3 Ray trace of split-field radiation path.

IV. IMAGE ACQUISTION AND ANALYSIS

To prove the concepts presented and to demonstrate the effects of polarized filtering on image contrast, it is necessary to perform image analysis on images recorded with the thermal imaging system in three configurations; (a) thermal imager only, (b) external polarization and (c) split-image optical system polarizing. Laboratory experiments were set up to demonstrate the system performance.

A. EQUIPMENT SET UP

The equipment necessary for these experiments are the Cincinnati 3-5 μm waveband thermal imager, external polarizer, the split field polarimeter, monitor, computer and a frame grabber.

The experiment set up is such that the thermal imager is looking at the target (a heated rectangle block) at or near the Brewster angle. As explained in Chapter II, at this angle the reflection and the emission radiation will exhibits some form of polarization characteristic. The output of the thermal imager is connected to the monitor for visual monitoring and in parallel to the frame grabber for image acquisition. The acquisition software is provided by the frame grabber manufacturer. Post processing and image analysis is then done on the acquired images. Figure 4.1 depicts the experiment set up using the Cincinnati thermal imager with the split-field polarimeter. The set up for external polarizer with the thermal imager is similar; replacing the split-field unit with the external polarizer. The external polarizer is placed in front of the thermal imager with the help of a clamping device.

The following sections give a brief description of the critical components used in these experiments.

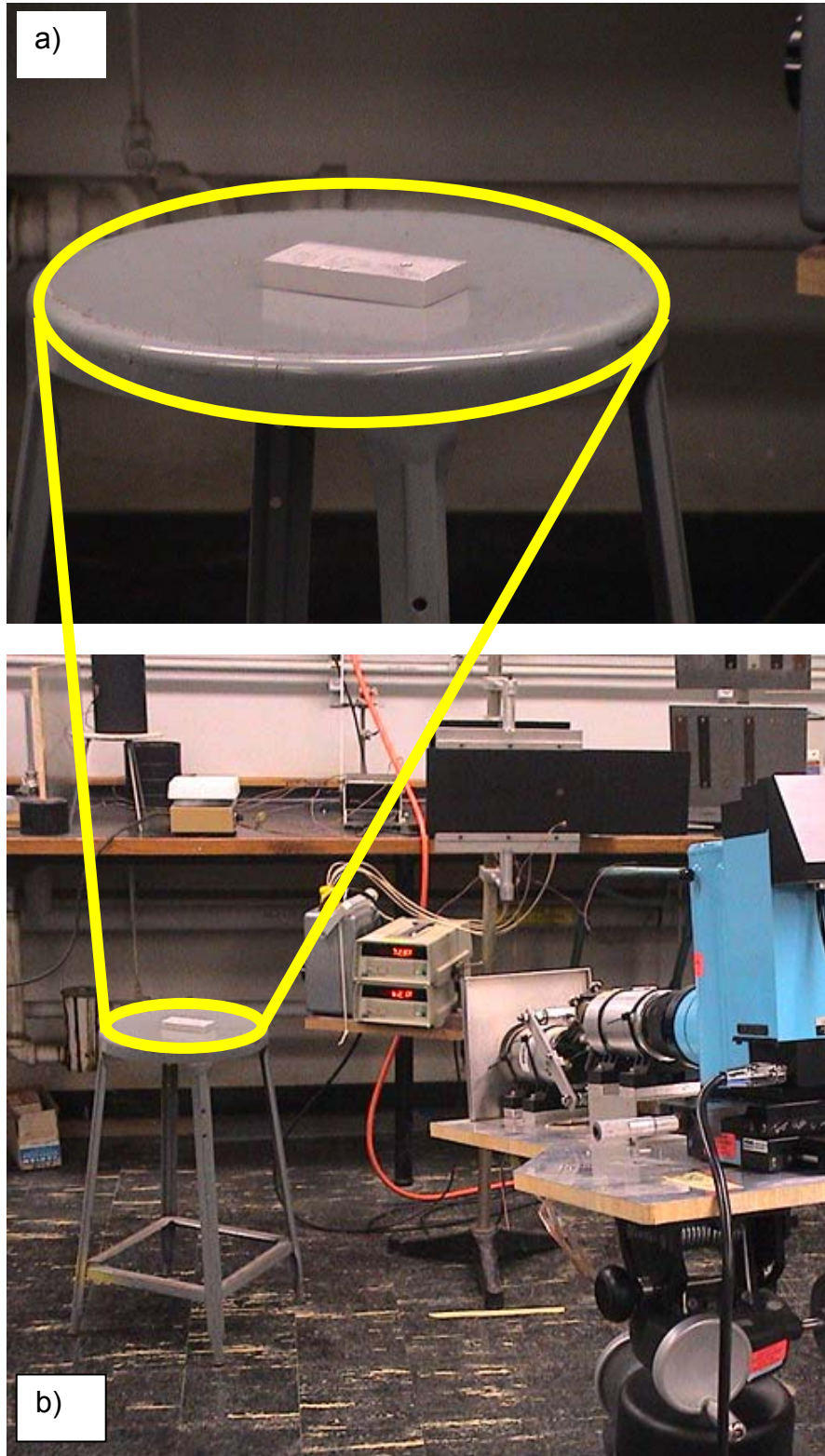


Figure 4.1 The laboratory set up for image analysis. (a) Detail of target in location, (b) Equipment in place for polarization testing.

1. The CINCINNATI Infrared Thermal Imager

The Cincinnati Electronics IRRIS-256LN is a generation III mid wave (3-5 μm) thermal imager as shown in Figure 4.2. It uses a hybrid Focal Plane Array (FPA) with 256 X 256 Indium Antimonide (InSb) detectors on a silicon substrate, and on-chip multiplexing. This system is cooled to 77K using liquid nitrogen. InSb has a relatively high quantum efficiency (typically around 80%), and is relatively sensitive, with a 0.025K temperature sensitivity, and 0.6 milliradian spatial resolution (with the standard lens). The hybrid structure is difficult to manufacture, and the uniformity of the detector elements is low.



Figure 4.2 The Cincinnati IRRIS-256LN Thermal Imager.

2. External IR Polarizer

The simplest polarizing device is a grid of parallel conducting wires, as shown in Fig 4.3.

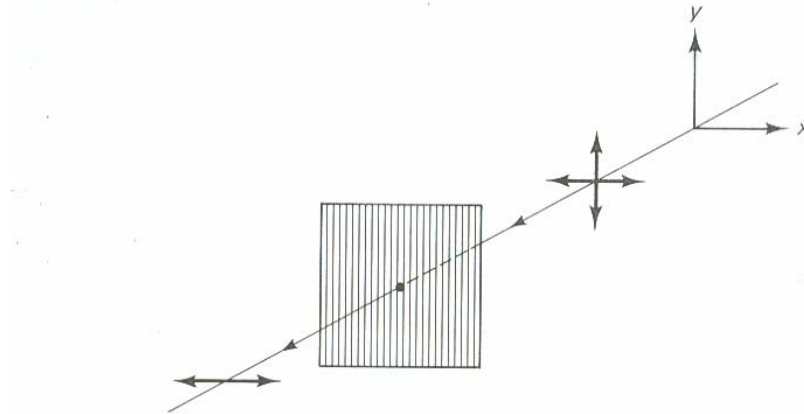


Figure 4.3 General output of a typical wire grid polarizer.

The y-component of the field generates a current along the length of each wire in the grid by accelerating the electrons in the direction of the electric field. The current subsequently heats the wires as a result of collision or joule heating causing absorption. The electrons accelerating along the y-axis radiate in both the forward and backward directions. The result is a cancellation of the incident wave by the radiated wave in the forward direction and thus no transmission of the y-component of the electric field. The radiation propagating in the backward direction simply appears as a reflected wave. In contrast, the electrons are not free to move very far in the x-direction, and the corresponding field component of the wave is essentially unaltered as it propagates through the grid. The axis of the transmitted radiation is perpendicular to the wires in the grid. Proper function of the wire grid as a polarizer requires that the space between the wires be no greater than the wavelength of light to be polarized.

3. Frame Grabber

The Image acquisition is via the PCMCIA VCE-B5A01 frame grabber as shown in Fig 4.4. It is a low cost, high performance, plug and play CardBus video capture card. It allows users to display, capture, store, and preview motion video on their notebook computers. VCE-B5A01 is capable of capturing single frame, multiple frames, and standard AVI clips from a variety of NTSC, PAL or SECAM sources. Each captured frame can be stamped with a user message along with the date and time of capture. These features allow users to turn their notebooks into a mobile observation system.



Figure 4.4 VCE-B5A01 PCMCIA Frame Grabber Card.

B. IMAGE ANALYSIS

1. Thermal Imaging Using External IR Polarizer

Figure 4.5 depicts the rectangular block being the object of interest used in the image analysis for the various configurations of imaging using different orientation using polarizing filters and with the split-field polarimeter.

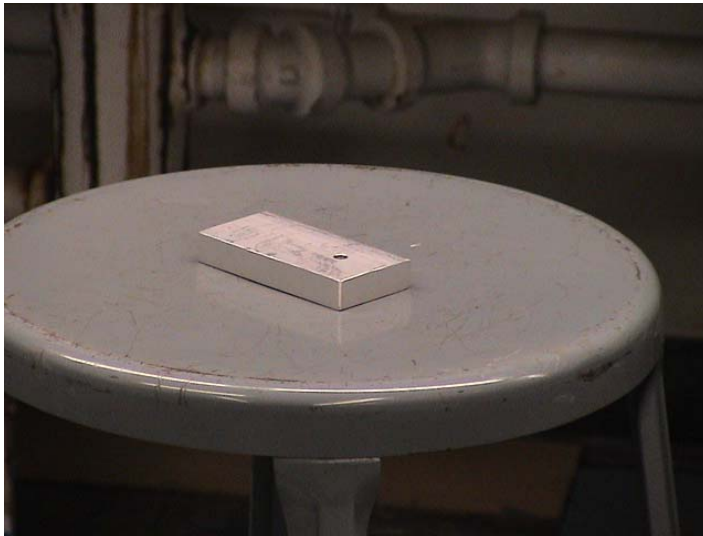


Figure 4.5 The image of the target in the visual waveband.

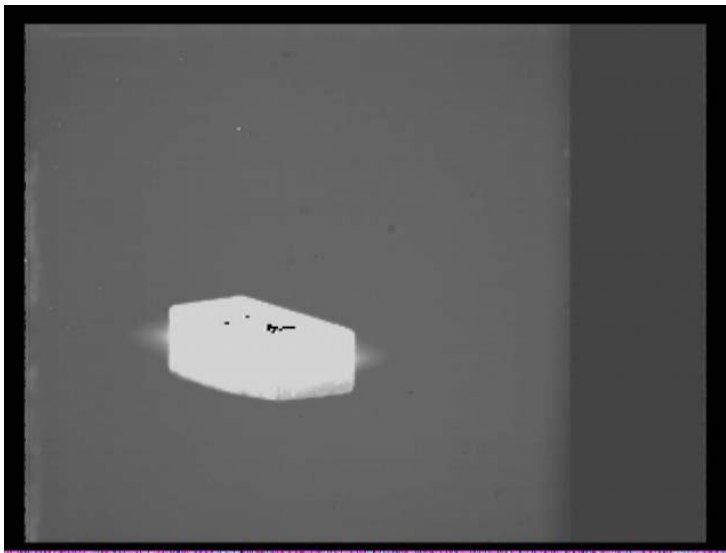


Figure 4.6 The image of the target in the 3-5 μm waveband.

Fig 4.7 and 4.8 depicts the thermal image of the horizontal and vertical polarization respectively.

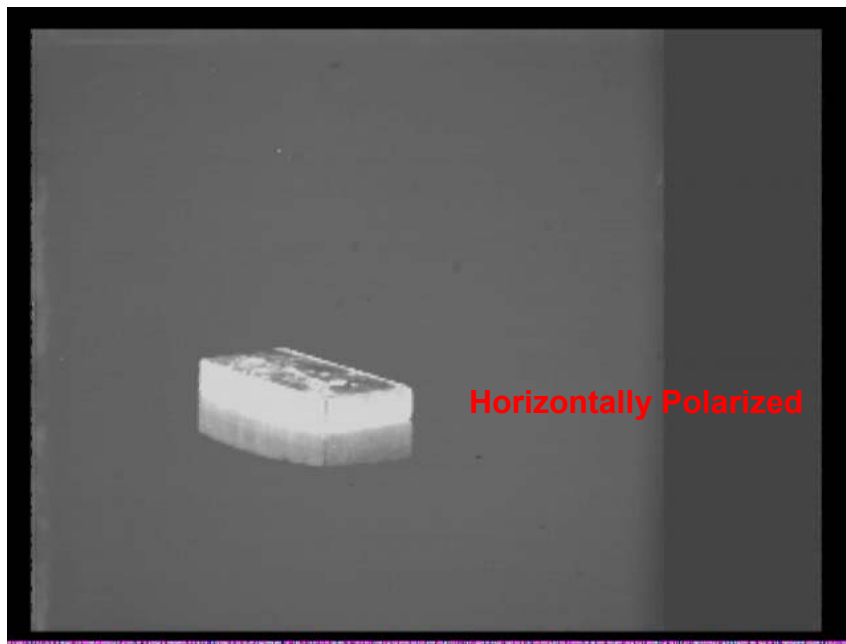


Figure 4.7 Image of the target filtered by a horizontal polarizer.

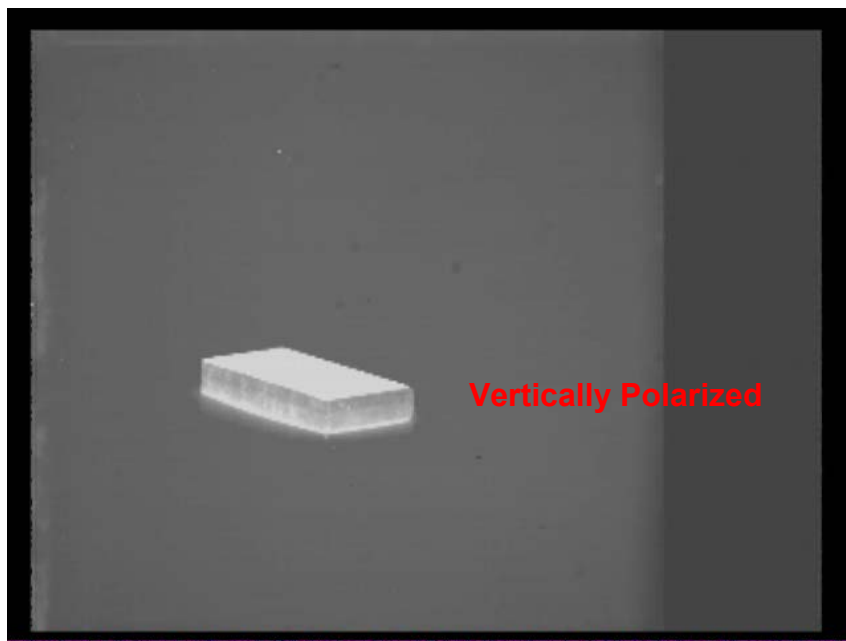


Figure 4.8 Image of the target filtered by a vertical polarizer.

Using visual analysis, both the horizontal and vertical polarized images as shown in Figure 4.7 and 4.8 depict their own characteristics. The images show that the contrast from the top face of the block is brighter when viewed through the vertical polarizer. This shows that the top surface is predominantly vertically polarized. The contrast from the side of the block is brighter when viewed through the horizontal polarizer. This shows that the side of the block is predominantly horizontally polarized.

The top face and the side of the rectangular block are orthogonal. The vertically polarized component on the top face with reference to the normal of the top face and the horizontally polarized components on the side of the block with reference to the normal of the side are in the same orientation reference to the polarizer. Therefore a vertical polarizer filter will filter the horizontal component from the top face and the vertical component from the side. Likewise, the horizontal polarizer will filter the vertical component from the top face and the horizontal from the side. This infers that the bright contrast is the contribution of the vertical component with respect to the normal of that plane.

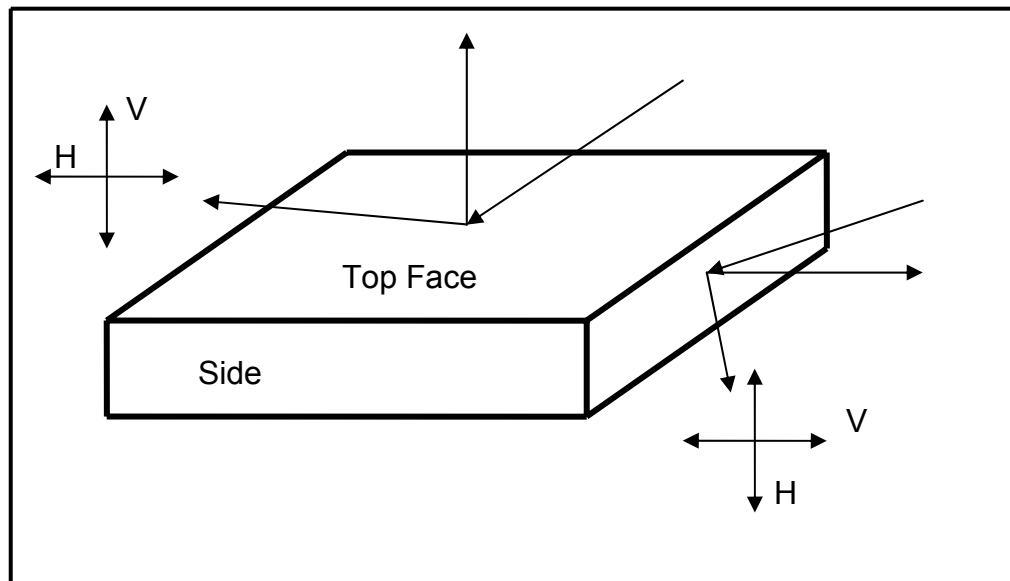


Figure 4.9 Schematic of the horizontal and vertical components for both the top face and the side.

The reflection of the block is depicted in Fig 4.6 (without polarizer) and again in Fig 4.7 (horizontally polarized) but at a lower contrast, whereas in Fig 4.8 (vertically polarized) the reflection is filtered. This phenomenon shows that the reflected infrared radiation of the block is predominantly horizontally polarized.

Both the horizontal and vertical polarizer filtered out the background noise and enhanced the information of the surface of the block. It is noted that the texture on the top of the block is enhanced using the horizontal polarizer while the grain on the side of the block is enhanced using the vertical polarizer. The vertical polarizer also filters out the reflected radiation, hence the outline of the block is enhanced.

This simple experiment demonstrates that for man-made object of different shapes both its emitted and reflected infrared radiation produce linearly polarized components.

2. Thermal Imaging Using Split-field Polarimeter

The same experiment is carried out using the split-field polarimeter. All the specifications such as the block temperature, the viewing angle of the thermal imager and the distance between target and thermal imager remains the same. This is necessary for a meaningful comparison between the two experiments.

The image of the target viewed through the split-field polarimeter is depicted in Fig 4.9. The top image is the horizontally polarized whereas the bottom image is vertically polarized. Both the horizontal and vertical polarized images show almost identical phenomena to the external polarizer.

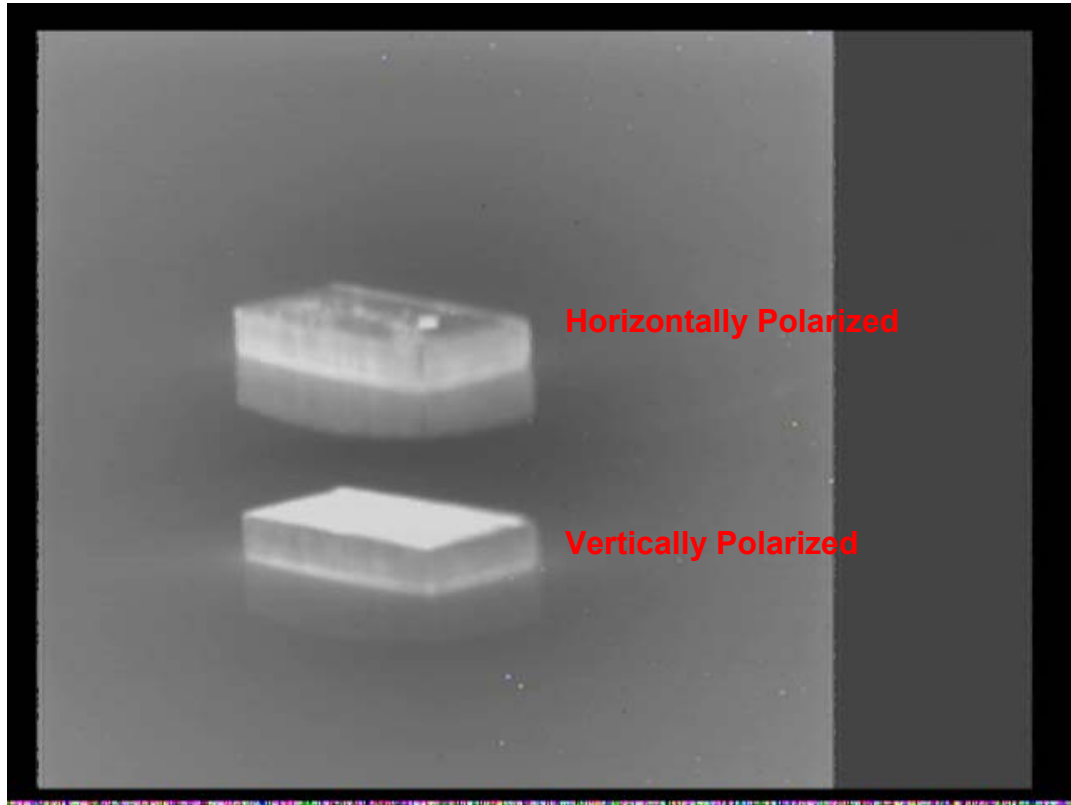


Figure 4.10 Image of the target viewed through the split-field polarimeter.

This experiment verifies that the split-field polarimeter works with the new 3-5 μm beam splitter. The mirrors in the split-field polarimeter are adjusted so that the horizontal and vertical images are aligned.

With the functionality of the split-field polarimeter verified, it is necessary to measure its performance. This is done by means of measuring the system minimum resolvable temperature difference (MRTD).

V. MINIMUM RESOLVABLE TEMPERATURE DIFFERENCE

Minimum resolvable temperature difference (MRTD) is a static performance prediction methodology for thermal imagers. MRTD is a noise limited threshold measure of system spatial resolution and thermal sensitivity which includes the characteristics of the human operator. As an operator is in the test loop, it is a subjective measure of thermal imager performance. MRTD is defined as the temperature difference between a uniform background and the bars of a four bar pattern, each bar having 7:1 aspect ratio (so the overall pattern will be a square), which is required by a trained observer to just resolve all four bars when viewing the pattern through the imager. The results depend on decisions made by an observer and the results vary with training, motivation, and visual capacity.

A. LABORATORY SETUP

The laboratory setup for the MRTD measurement for the various configurations (with and without the external polarizer and with the polarimeter) is shown in Figure 5.1. It required the use of a four bar target, an external infrared polarizer, the split-field optical equipment, the Cincinnati infrared thermal imager, oscilloscope and a computer with frame grabber. The oscilloscope is used to measure the TV signal of the target as a second reference to the operator as to the least contrast temperature difference which one can discern in the picture. The objective is to derive an objective measurement threshold by means of the signal waveform as opposed to the subjective measurement which is determined by the observer decision. The computer with the frame grabber card is used to capture the target image for analysis.

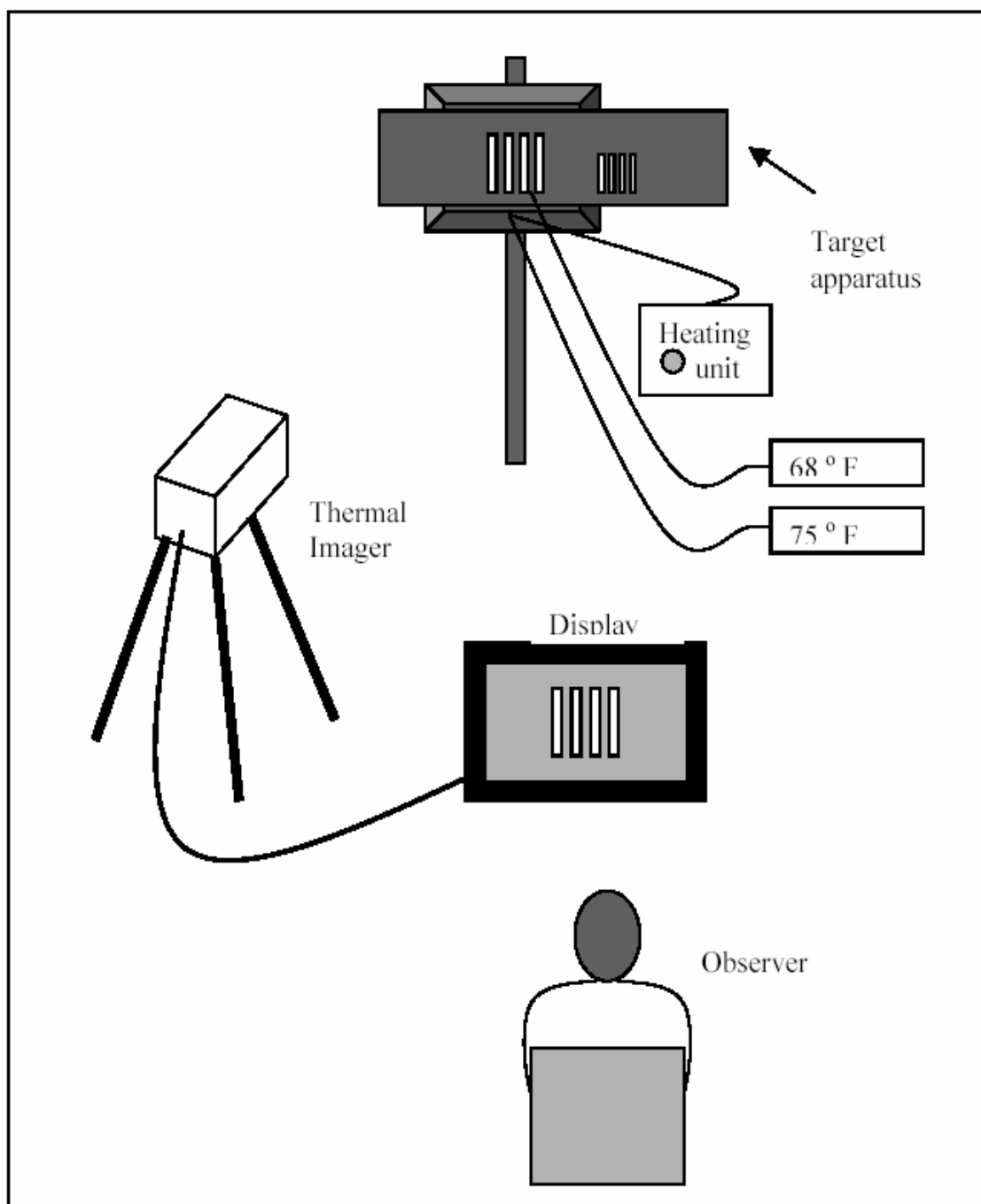


Figure 5.1 Laboratory setup for the measurement of MRTD

1. Four Bar Target

The four bar target as shown in Fig 5.2 consists of a heated plate (back plate) of which the temperature is regulated. This is done by applying a variable voltage across a resistance installed on the backside of the plate. In front of the heated plate is a background plate in which a standard four slot MRTD pattern is machined. Each bar has an aspect ratio of 7 is to 1. Hence with 4 bars and three spacers, the target is a square. The four bar target enables the heat from the black plate to radiate through the slots. With a set of targets of different dimensions, we can create the different spatial frequencies for the measurements. Temperatures of the two plates are measured using thermocouples with digital readings. The difference of the two measurements is the target background temperature difference for the MRTD measurement.

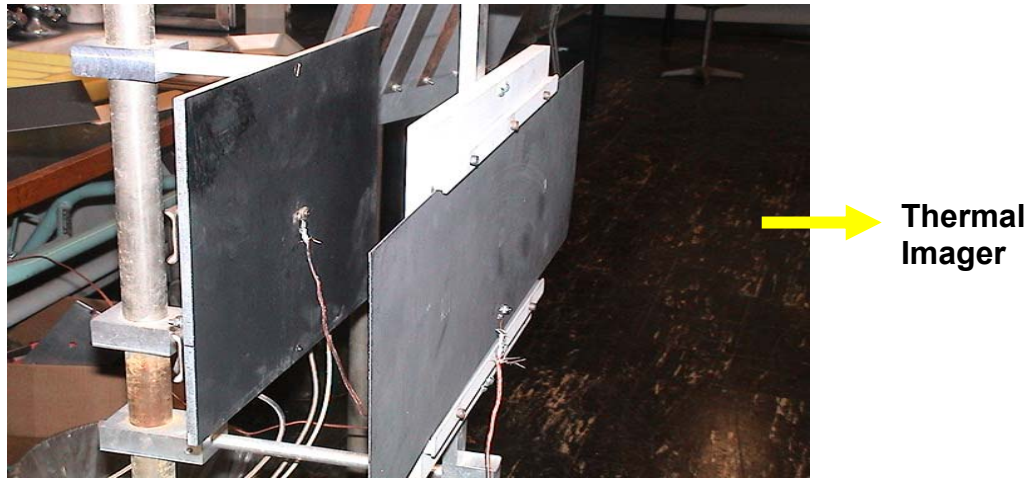


Figure 5.2 The back and front plates of the four bar target.



Figure 5.3 The front side of the four bar target

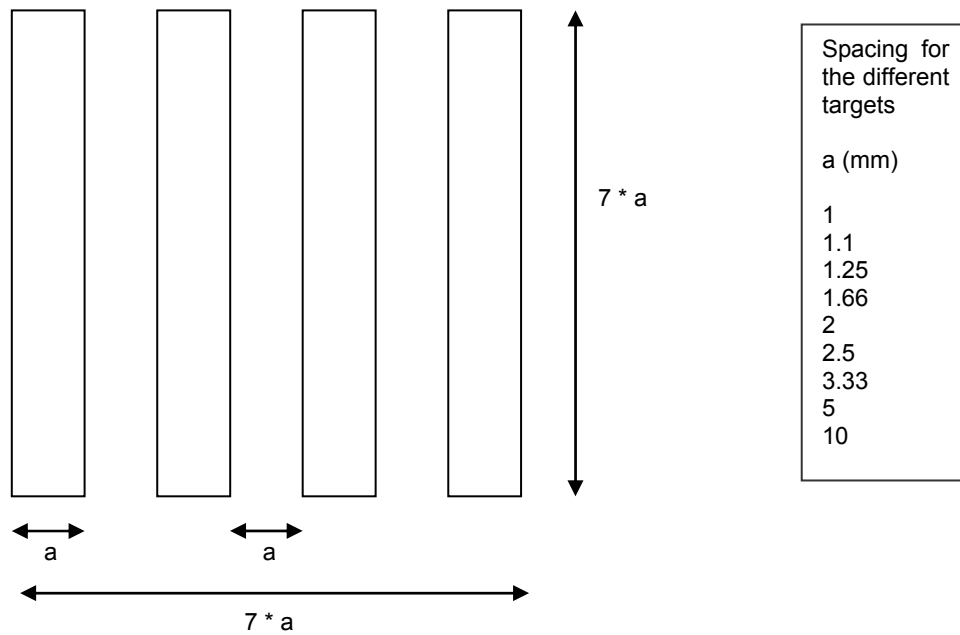


Figure 5.4 MRTD pattern.

B. MRTD MEASUREMENTS

The laboratory setup is shown in Fig 5.1. The observer is allowed unlimited viewing time and can continually adjust the system gain and level to optimize the image for his detection criterion. Likewise, the observer can adjust the monitor contrast to enhance the image contrast. The ambient lighting should approximately match the monitor luminance. The observer must be allowed sufficient time to dark adapt to the reduced ambient lighting before proceeding with the test. It is important that the observer not be influenced by the environment such as extraneous light sources, and other people in the room.

The entire threshold detection versus spatial frequency curve should be measured. Because a discrete target is used, the location at which the MRTD asymptotes to infinity may not be measured. The curve may asymptote between the last resolvable target and the next available target.

The measurement starts with the highest spatial frequency target as the temperature difference is expected to be the highest. This is known to us from many infrared literature sources. The infrared camera is placed at a measured distance from the target. The size of the target and the distance between the target and camera will determine the spatial frequency in cycles per milliradian. The image of the target is then viewed on the monitor display. Once the target is not resolvable (that is, the observer cannot discern the four bar target) the temperature difference is recorded for that spatial frequency target. This procedure is repeated for different spatial frequency targets. Figure 5.5 depicts three images of the four bar pattern ranging from one that is resolvable to one that is not resolvable. For the bottom image, the monitor contrast is tuned to the maximum; even then, the four bar pattern is not resolvable.

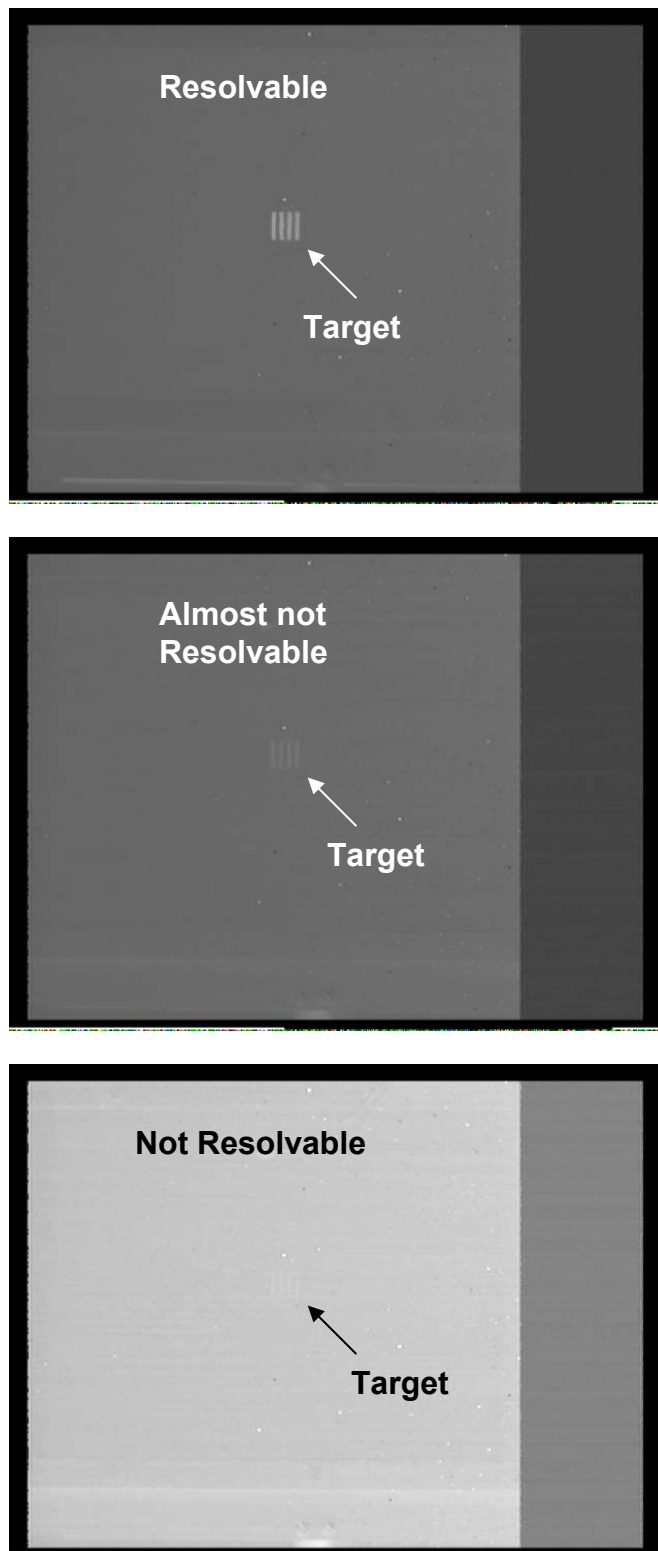


Figure 5.6 Sequence of images from resolvable to not resolvable.

Measurement of MRTD requires an experienced operator, as the ability to discern the four bar target has a great bearing on the performance measurement of the system. System training to gain experience in such measurement is necessary to make the measurement results meaningful. Without the possibility of having many operators to perform this experiment, the measurement is repeated several times on different dates. The consistency appears only after the third set of measurements. Consistency between individual observers is not assured by this procedure.

A typical MRTD plot with the corresponding spatial frequency four bar targets inserted is shown in Fig 5.7. The results in the experiment should take this form. The curve approaches an asymptote as higher and higher spatial frequency targets are used. The asymptote of the MRTD curve determines the system resolution limit.

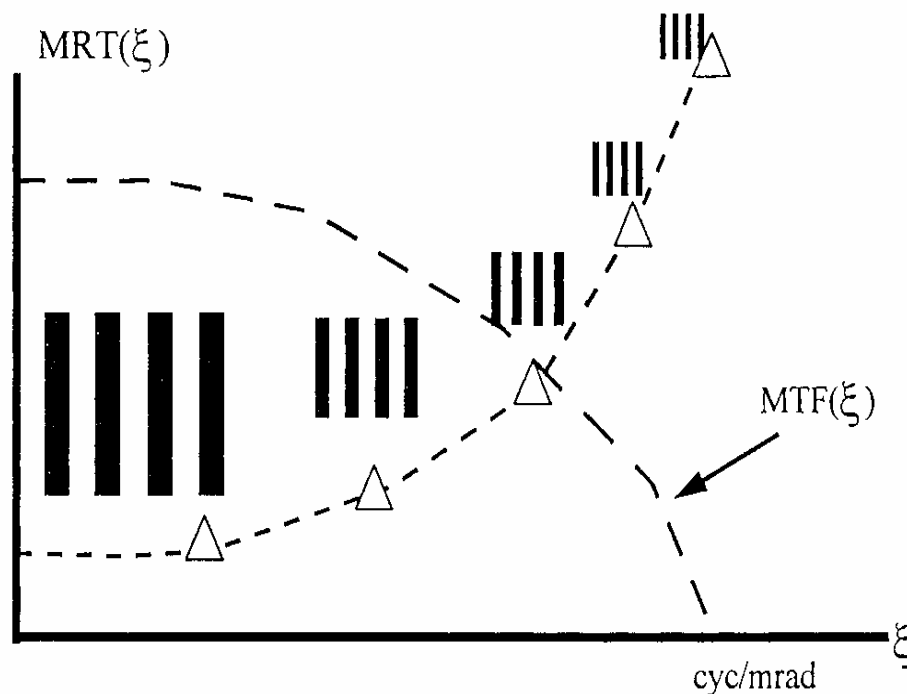


Figure 5.7 MRTD plot.

THIS PAGE IS INTENTIONALLY LEFT BLANK

VI. MRTD RESULTS AND ANALYSIS

A. THERMAL IMAGER MRTD

The measured MRTD data for the thermal imager is tabulated in Table 6.1. A MATLAB program is written to plot the measured results. The program then generates the best fit curve as shown in Fig 6.1.

Target No	Spatial Frequency (mrad) ⁻¹	ΔT (°C)
15	1	0.11
16	0.94	0.22
17	0.89	0.27
18	0.8	0.33
19	0.67	0.44
20	0.57	1.55
21	0.44	1.77

Table 6.1 Measured MRTD data of thermal imager.

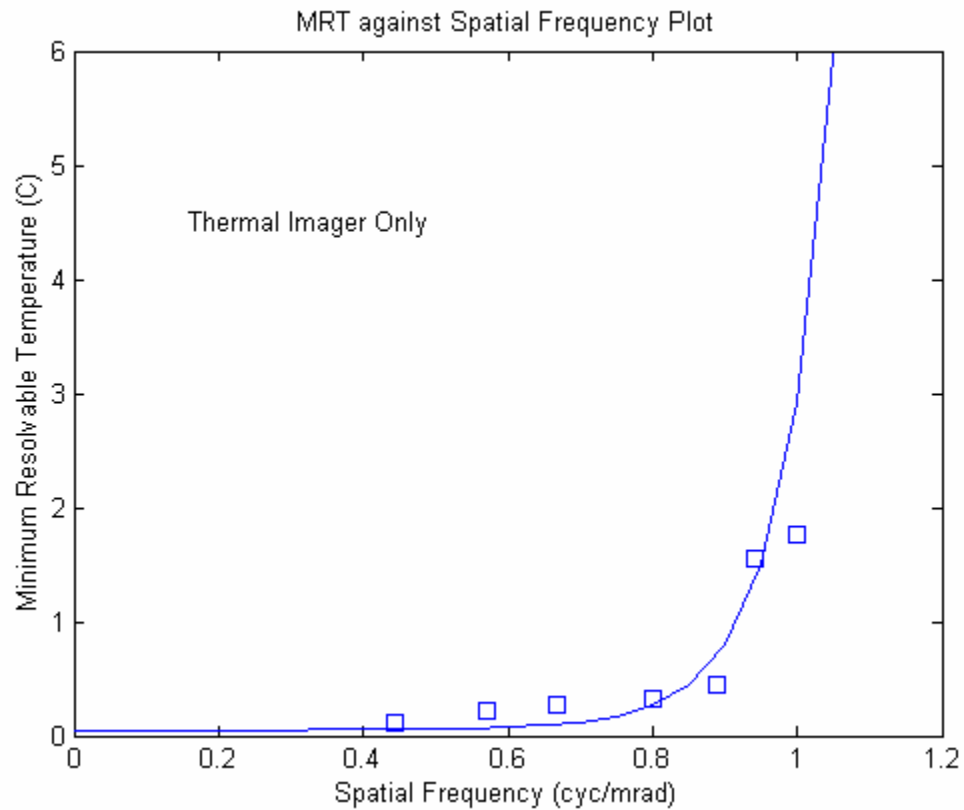


Figure 6.1 Thermal imager MRTD plot.

From Fig 6.1 it is noted that the thermal imager has a sensitivity of 0.3°C up to spatial frequency of 0.9 cycles per mrad. The asymptote of the functionally fitted curve determines the system resolution limit which is 1.05 mrad.

B. THERMAL IMAGER WITH EXTERNAL POLARIZER MRTD

The MRTD measurement data for the thermal imager with external polarizer is tabulated as shown in Table 6.2. The same MATLAB program is used to plot the measured results and also to generate the best fit curve.

Target No	Spatial Frequency (mrad) ⁻¹	ΔT (°C)
15	1	0.28
16	0.94	0.33
17	0.89	0.38
18	0.8	0.5
19	0.67	0.55
20	0.57	3.11
21	0.44	3.5

Table 6.2 Measured MRTD data of the thermal imager viewing through the external polarizer.

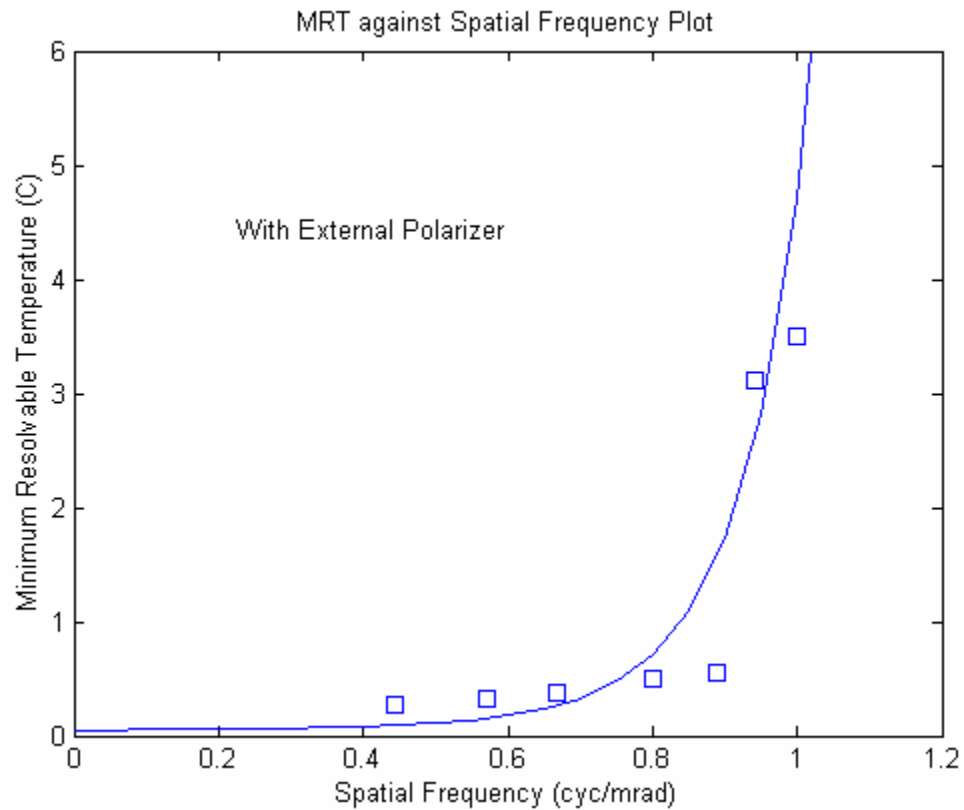


Figure 6.2 Thermal imager with external polarizer MRTD plot.

From Fig 6.2 it is noted that the thermal imager with external polarizer has a sensitivity of 0.5°C up to spatial frequency of 0.80 cycles per mrad. The asymptote of the fitted curve determines the total system resolution limit which is 1.02 mrad.

C. THERMAL IMAGER WITH SPLIT FIELD POLARIMETER

The MRTD measurement data for the thermal imager with the split field polarimeter is tabulated. Again the same MATLAB program is used to plot the measured results and generate the best fit curve.

Target No	Spatial Frequency (mrad) ⁻¹	ΔT (°C)
15	1	1.38
16	0.94	2.16
17	0.89	2.77
18	0.8	3.33
19	0.67	3.77
20	0.57	4.27
21	0.44	5.0

Table 6.3 Measured MRTD data of thermal imager viewing through the split-field polarimeter.

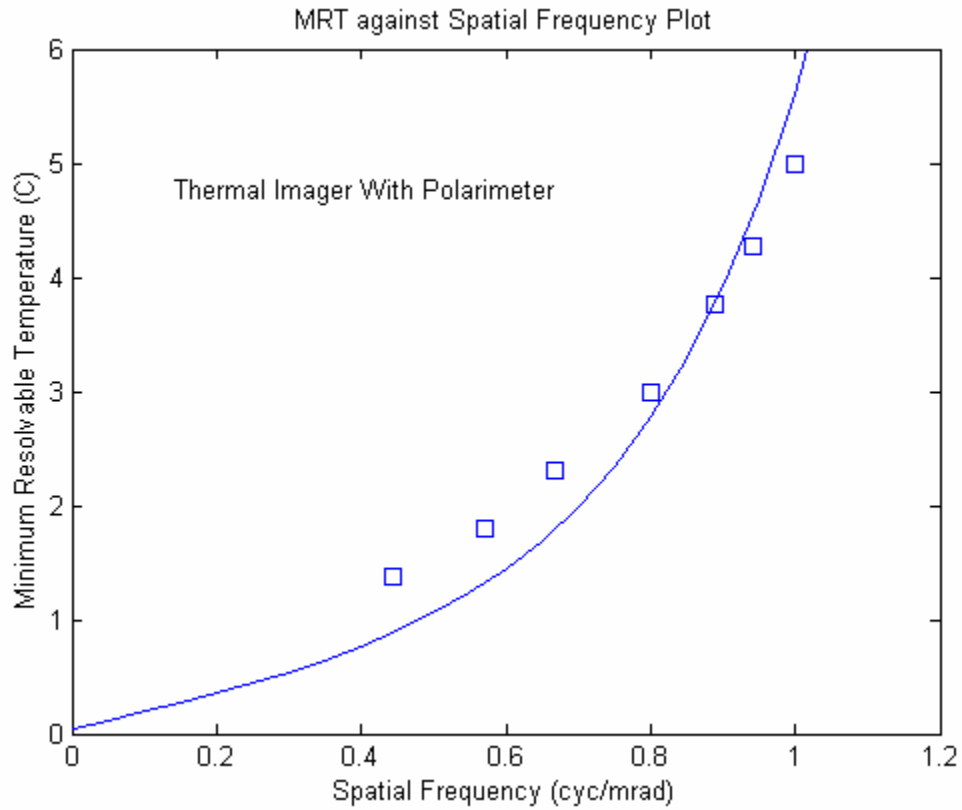


Figure 6.3 Thermal imager with split field polarimeter MRTD plot.

From Fig 6.3 it is noted that the thermal imager with split field polarimeter has a sensitivity of 4°C at spatial frequency of 0.9 cycles per mrad. The asymptote of the curve determines the total system resolution limit that is about 1.01 mrad.

D. MRTD MEASUREMENT ANALYSIS

The three MRTD plots are merged into a single plot as depicted in Fig 6.4.

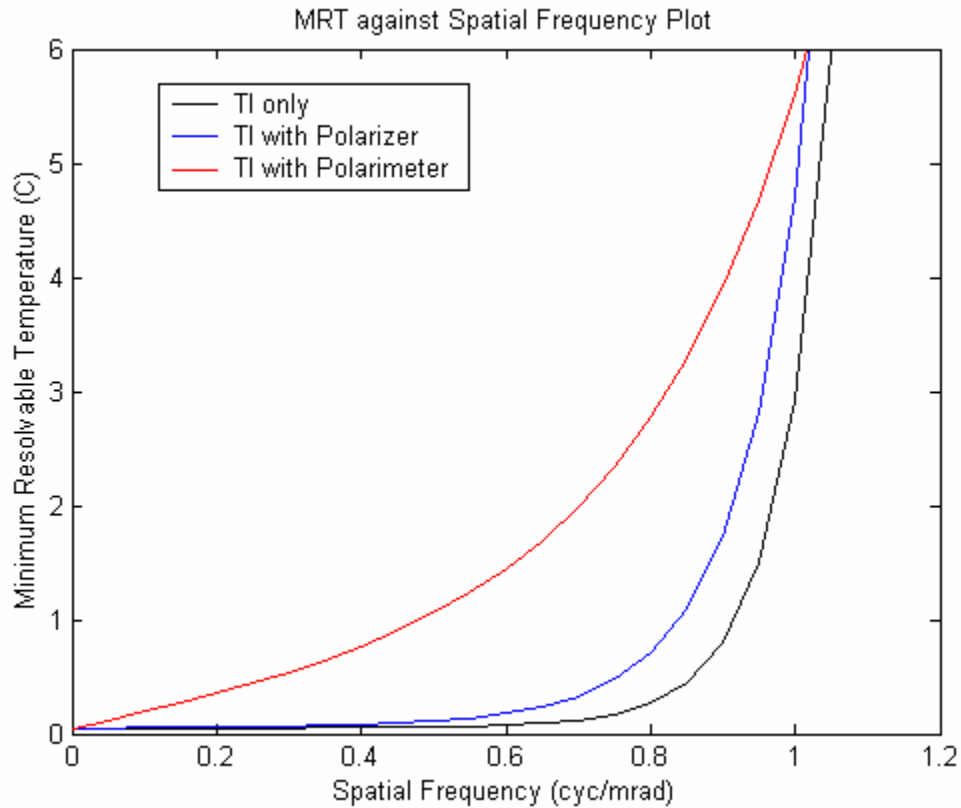


Figure 6.4 The MRTD plots of the three configurations.

The above plot clearly shows that with the increase in the number of components added to the thermal imager both the sensitivity and the resolution limits of the total system decrease. This is reasonable as when more optics is added the transmittance of the system is reduced, hence both the sensitivity and resolution are diminished.



Figure 6.5 Thermal imager with external polarizer.

Figure 6.5 depicts the thermal imager with the external polarizer in front of its lens. The Modulation Transfer Function (MTF) of the total system is then degraded by only the single component. The effect on both the sensitivity and resolution is minimal. However, there is a significant chance of Narcissus.

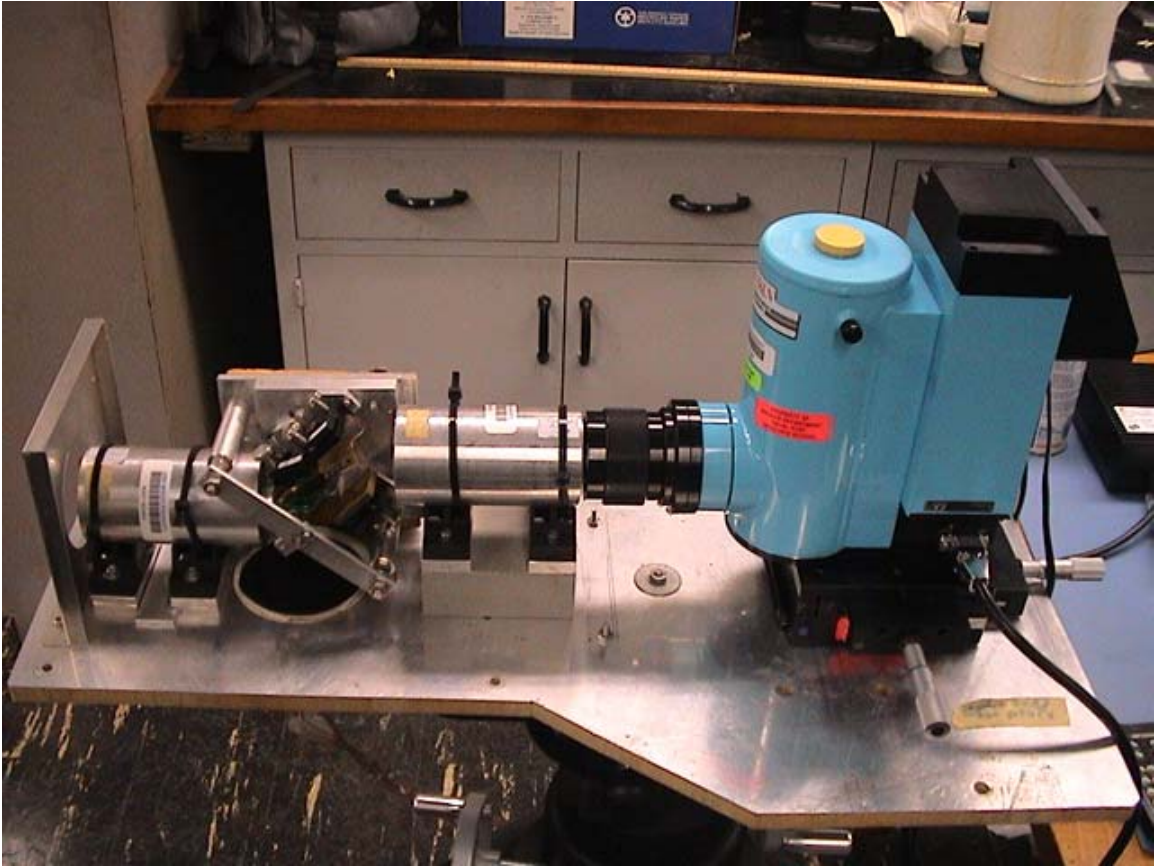


Figure 6.6 Thermal imager with split field polarimeter.

Figure 6.6 depicts the thermal imager with the split field polarimeter. The optics in the optical path has increased and hence we would expect the transmittance of the optical path to be lower due to higher reflection losses in the optical system. This will degrade the MTF of the total system further. Hence the sensitivity and the resolution are further degraded as compared to the thermal imager with external polarizer.

The other source that affected the degradation in the sensitivity of the system is the thermal radiation emitted by the 4 uncooled mirrors and the splitter. Each is emitting as a gray body and contributes to the background noise. Therefore the minimum temperature required to discern the four bar target increases which translates into decrease in sensitivity.

The cold plate as indicated in Fig 5.7 is designed only to minimize the reflection of the ambient noise from the lower side of the splitter into the system. However the radiation from the mirrors cannot be eliminated unless the entire system is enclosed in a nitrogen filled housing and cooled. The current fixture is not able to do that.

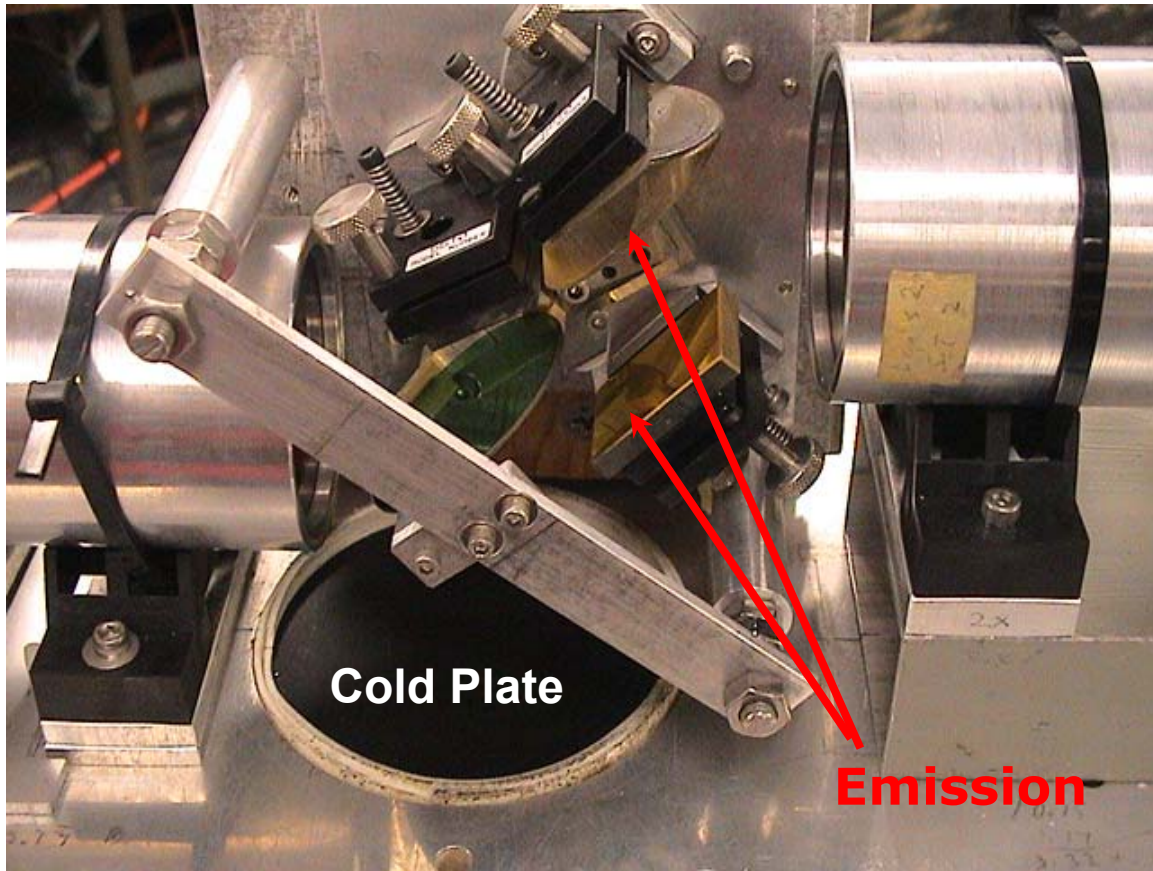


Figure 6.7 Radiant emission from the reflecting mirrors.

E. RANGE PREDICTION

1. Johnson Criteria

In the late 1950s John Johnson investigated the relationship between the ability of an observer to resolve a bar target through an imaging device and their ability to perform the tasks of detection, recognition, and identification of military vehicles through the same imager. It is worthwhile to review his experiment briefly, along with what has become known as the equivalent bar pattern approach.

In the laboratory, scale models of eight different vehicles and one soldier were placed against a bland background. Observers viewing the targets through image intensifiers were asked to detect, determine the orientation of, recognize, and identify the target. Air Force bar charts whose bars had the same contrast as the scale targets were also viewed through the same imager, and the maximum resolvable bar pattern frequency was determined as a function of contrast of the target. The maximum number of resolvable cycles across the target critical dimension was determined for each different task using

$$N = H_{\text{target}} \times f_x \quad (6.1)$$

where

N = the number of just resolvable cycles across the target critical dimension

H_{target} = the critical dimension of the military target in milliradians, usually chosen to be the minimum dimension, which for tactical army vehicles is often the height

f_x = the highest resolvable bar pattern fundamental spatial frequency in cycles per milliradian

Table 6.4 shows the results of the experiment in which it was found that the number of just resolvable line pairs across the minimum dimension of the target required to perform a particular discrimination task was within 25% of a fixed number of cycles. As long as the bar target contrast equaled the target-to-background contrast, the resulting number of cycles was found to be independent of target-to-background contrast and scene light level. In this manner the ability of an observer to perform discrimination tasks was related to the ability of the observer to resolve bar patterns. Therefore, the prediction of the discrimination performance of the observer looking through an electro-optic (EO) device was simplified to the prediction of their ability to resolve bar patterns through the EO system.

Target	Resolution per Minimum Dimension			
Broadside view	Detection	Orientation	Recognition	Identify
Truck	0.90	1.25	4.5	8.0
M-48 tank	0.75	1.2	3.5	7.0
Stalin tank	0.75	1.2	3.3	6.0
Centurion tank	0.75	1.2	3.5	6.0
Half-track	1.0	1.5	4.0	5.0
Jeep	1.2	1.5	4.5	5.5
Command car	1.2	1.5	4.3	5.5
Soldier	1.5	1.8	3.8	8.0
105 Howitzer	1.0	1.5	4.8	6.0
Average	1.0	1.4	4.0	6.4

Table 6.4 Number of cycles required across target's critical dimension for various discrimination tasks. From [Ref. 17].

Results of several field tests using thermal imagers have been used to establish what has been termed the target transform probability function (TTPF). Johnson reported in Table 6.4 what was essentially the 50% probability point (referred as N_{50}) on a curve defining what portion of an ensemble of observers was able to perform a particular discrimination task. The shape of the TTPF curve can be approximated by

$$P = \frac{(N/N_{50})^E}{1+(N/N_{50})^E} \quad (6.2)$$

where

$$E = 2.7 + 0.7 (N/N_{50})$$

The TTPF curve plotted as a function of N/N_{50} can be used for all discrimination tasks by simply associating a particular N_{50} with the 50% probability of performing a particular task. Such a curve is plotted in Fig 6.8.

Later field testing using thermal imagers indicated that the N_{50} for identification was closer to 8 cycles than 6.4 as determined by Johnson. This could be caused by several factors, perhaps primarily the differences between imager intensifiers and thermal imagers. It was also noticed that recognition tasks varied widely in difficulty so that N_{50} varied over the range of 3 to 4 cycles. This led to a distinction being made between “conservative” (4-cycle) and “optimistic” (3-cycle) recognition tasks. It should be stressed that these N_{50} values should only be taken as representative values. When an analyst wishes to predict the performance of a specific task they should make a judgment about the difficulty of the task and vary N_{50} accordingly.

For higher order discrimination tasks the procedure is essentially the same except that the number of resolvable cycles required is higher. The prediction methodology being described is general in that the recommendation cycle criteria are the results of averaging of test results incorporating several situations,

observer, clutter levels and target aspects. Predictions using this technique will not reflect the performance of a specific observer trying to discriminate a particular target signature; rather the prediction is of the performance of an ensemble of observers viewing a set of target signatures.

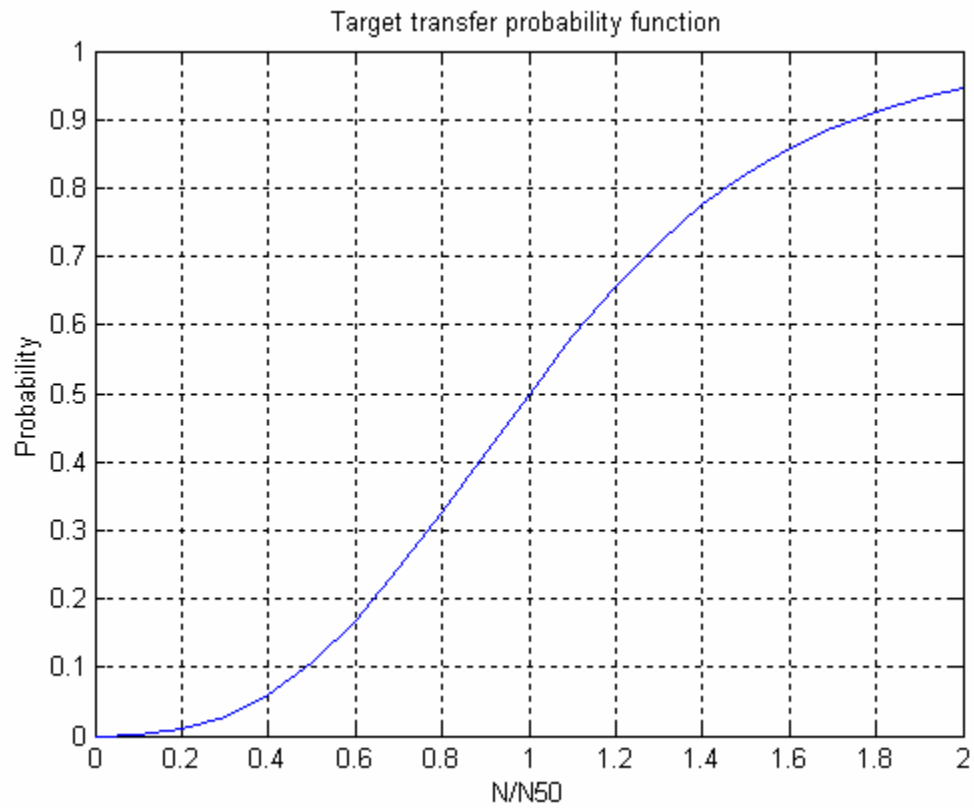


Figure 6.8 Target transfer probability function curve.

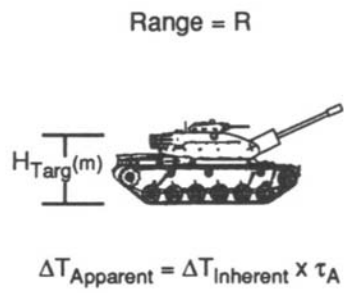
The steps involved in the discrimination prediction methodology are as follows:

- Determine the target critical dimension, range, and inherent ΔT .
- Calculate the apparent ΔT of the target at the range to the target, using knowledge of the atmospheric attenuation as a function of range.
- Calculate or measure the system MRTD. From the apparent ΔT and MRTD determine the maximum resolvable spatial frequency of the sensor at this apparent ΔT , f_x , in cycles per milliradian.
- Using the angular subtense of the target critical dimension, $\text{Height}_{\text{target}}/\text{Range}$, calculate the maximum number of resolvable cycles across the target, N , using

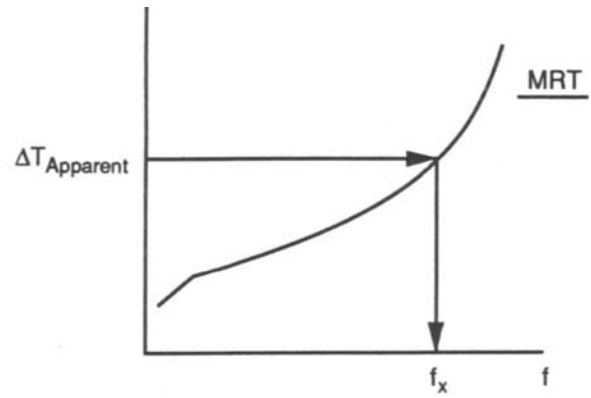
$$N = f_x \frac{\text{Height}_{\text{target}}}{\text{Range}} \quad (6.3)$$

- Determine the probability of performing a task from the TTPF curve.

This procedure is depicted schematically in Fig 6.9.



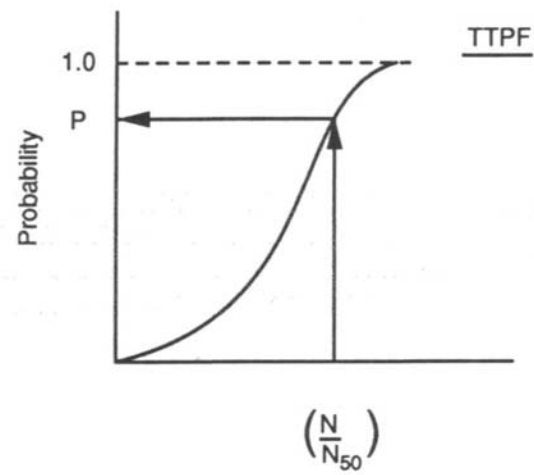
(a)



(b)

$$N = \frac{H_{Targ}}{R} f_x$$

(c)



(d)

Figure 6.9 Schematic diagram of the discrimination performance prediction methodology. From [Ref. 17]

2. System Prediction

Using the Johnson criteria methodology explained in the previous section, the maximum range for the specific task is estimated using the apparent target-background temperature difference (TBTD) and the measured MRTD in Fig 6.4 for the three configurations that is TI only, TI with external polarizer and TI with polarimeter. Although MRTD is a function of spatial frequency, we can translate it into a function of range, if specific target and task are given. Rearranging equation 6.3

$$\text{Range} = f_x \frac{\text{Height}_{\text{target}}}{N} \quad (6.4)$$

Figure 6.10 shows the MRTD plotted as a function of range for detection for a target with critical dimension of 15 m, and $N=1$ by the Johnson criterion for detection.

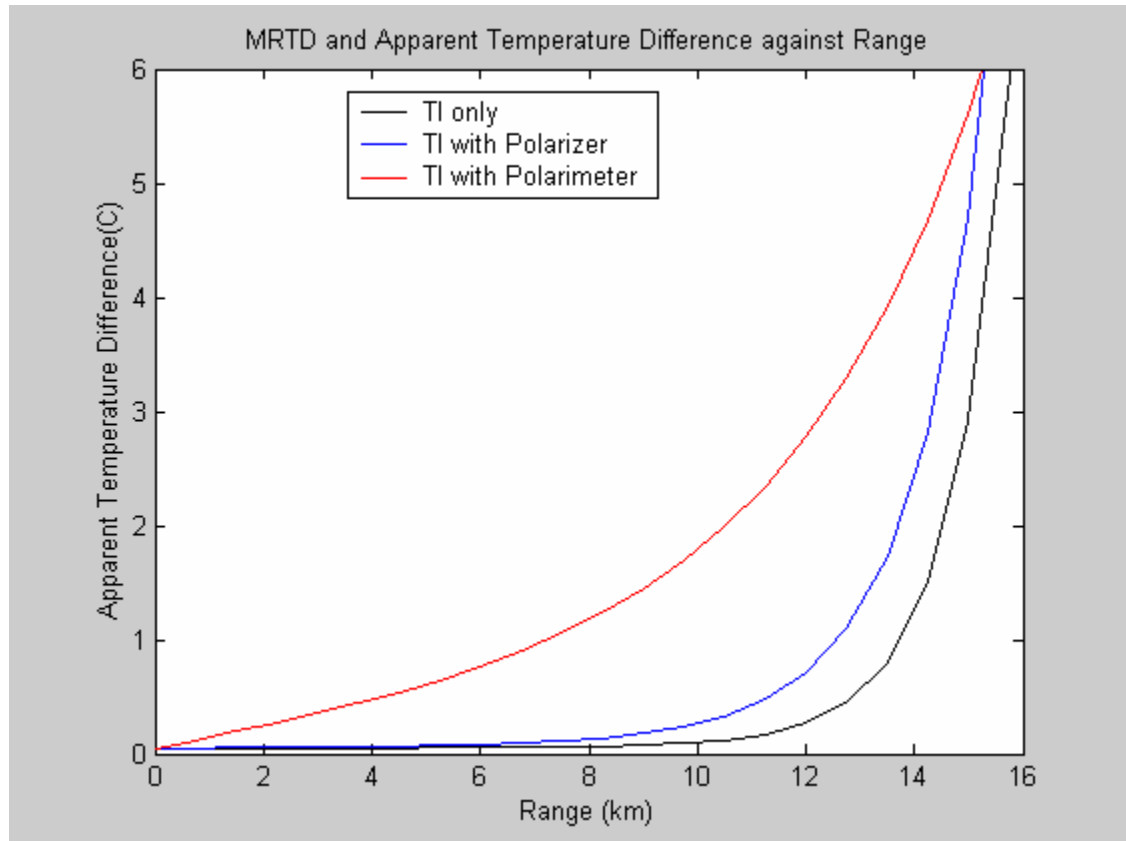


Figure 6.10 The MRTD as a function of Range. MRTD is for detection ($N_{50}=1$) with critical dimension 15 m.

The next step is to calculate the apparent temperature as a function of range. The computer code SEARAD is used to estimate the atmospheric transmittance for the following set of input parameters:

- Lowtran 7 was selected.
- Model: Mid-Latitude summer
- Type of atmospheric path: Horizontal path
- Surface albedo of earth: assumed Blackbody
- Navy maritime model
- No clouds or rain

- Wind speed: 4.10 m/s
- Wind speed: 4.10 m/s (24hrs average)
- Relative Humidity: 3
- Airmass character: 3
- Visibility: the program calculated visibility from the standard data for the Mid-Latitude summer.

With the transmittance factor estimated for the various ranges, the apparent temperature is determined by multiplying with the target to background temperature difference (TBTD) at source. Fig 6.11 depicts the apparent temperature difference as a function of range for a 10°C TBTD.

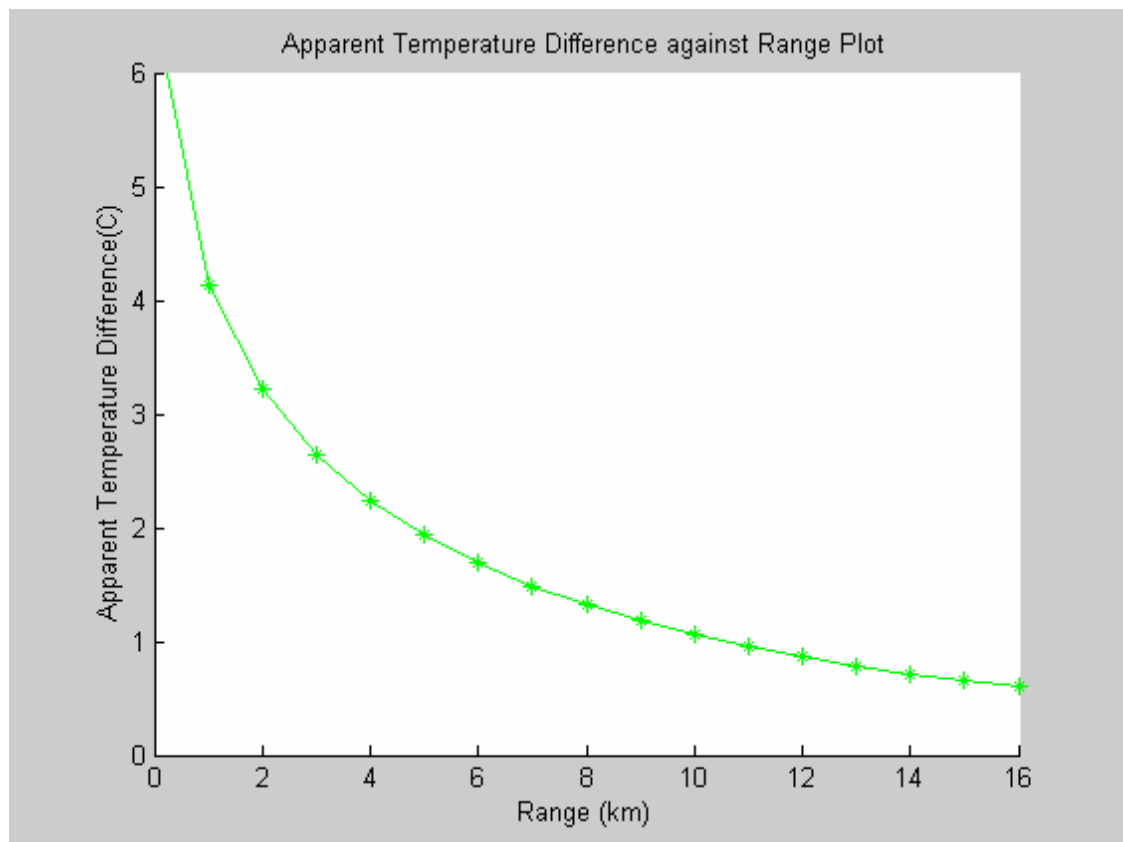


Figure 6.11 The Apparent Temperature Difference as a function of Range for a Temperature Difference at source of 10°C.

Figure 6.10 and 6.11 are merged into a single plot depicted in Fig 6.12. The intersection determines the maximum detection range for the three configurations.

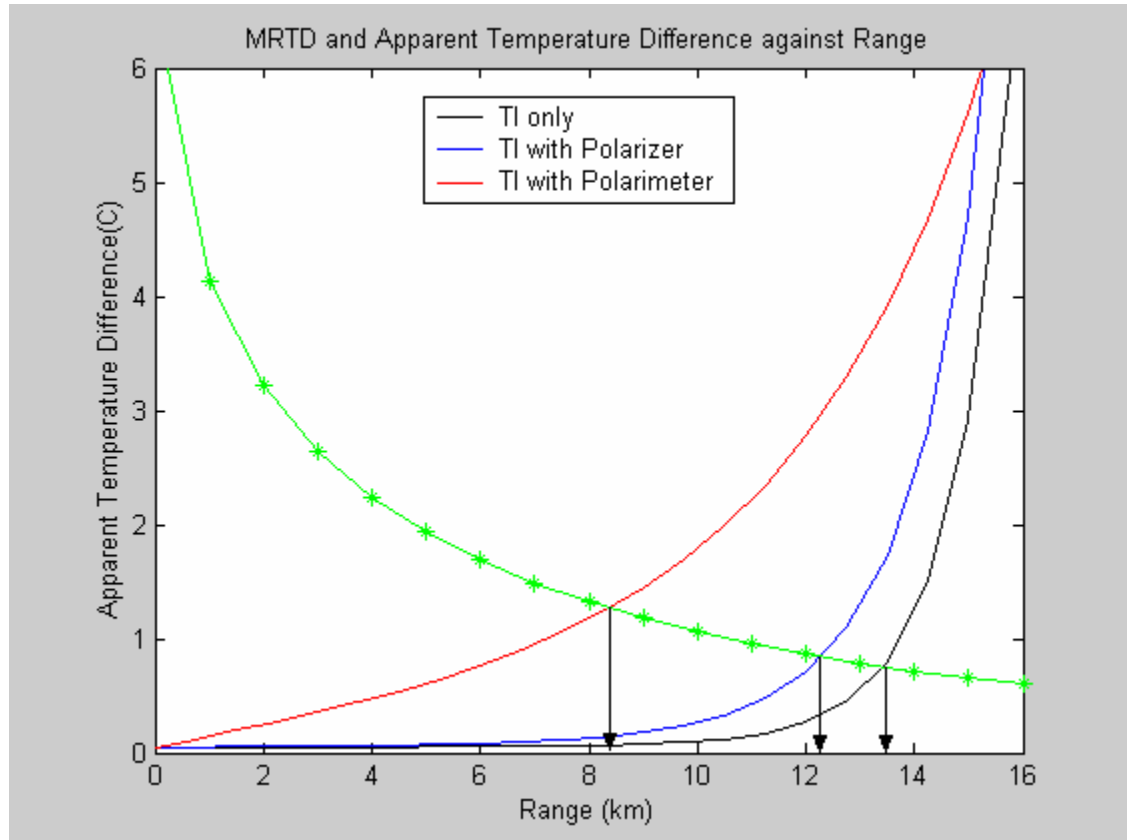


Figure 6.12 MRTD and Apparent TBTD as a function of Range for detection of a 15 m critical dimension target.

From the Fig 6.12, the maximum detection range for the thermal imager is 13.5 km; thermal imager with external polarizer is 12.3 km; and thermal imager with polarimeter is 8.4 km.

VII. CONCLUSIONS

The split-field polarizing system design and construction is once again proven. This work has demonstrated the polarimeter system operability in the 3-5 μm waveband.

Experiments conducted to visually compare the polarizing effect on objects in the 3-5 μm waveband using the polarimeter and with the external polarizer have shown positive results. The image recorded in the laboratory with the horizontal and vertical polarization depicts a different contrast enhancement for the different aspect of the target. Given the contrast enhancement, details of the texture are more distinct and hence provide more information of the object. The additional information in the real environment will enhance the mission operational capability.

With the successful demonstration of the polarimeter operability, the work is channeled to characterize the performance of the thermal imager operated with and without the polarimeter. This is done by means of measuring its Minimum Resolvable Temperature Difference (MRTD) at the different spatial frequencies. This is the standard yard stick in characterization of thermal systems. The MRTD measurement shows that the system resolution does not degrade much even with the added optics of the polarimeter to the thermal imager system. However the system sensitivity is significantly affected especially at the higher spatial frequency. The causes of this loss in sensitivity are due to the numerous factors which may need thorough investigation. These include:

- The two germanium anti-reflection coated aspheric lenses may have degraded over time and have caused reflection losses and scattered radiation.
- The radiation emitted from the gold mirrors and the lenses in the polarimeter has increased the background noise to the thermal imager, therefore decreasing the image contrast.

- The field of view of the polarimeter is 7° whereas the field of view of the Cincinnati thermal imager is 8.5° . Hence the thermal imager aperture is not fully utilized to receive the energy radiated from the target.

The MRTD measurement of the thermal imager polarimeter configuration is then compared against the same thermal imager using an external polarizer. The external polarizer configuration measured MRTD is quite close to the thermal imager only measurement. Even with one optic element in front of the thermal imager, some degradation is noted even though it is not appreciable.

Using the Johnson criteria model, SEARAD to estimate the atmospheric transmittance factor and the measured system MRTD; the system performance in terms of maximum detection range is estimated. The thermal imager with the polarimeter configuration due to its lower sensitivity the detection range is significantly lower than the thermal imager with external polarizer configuration. The difference between the maximum detection range of the thermal imager with and without the external polarizer is small. It must be emphasized that these predictions refer only to unpolarized target and unpolarized background.

Though the external polarizer configuration is better in sensitivity it has the problems of registration delay and narcissus.

The prediction thus far addresses only detection; the effect of polarization filtering the background noise to increase contrast and hence increase the detection range is not modeled. We would expect the range to a field target to increase with the polarizer, and therefore this prediction is conservative. However the choice and performance of the polarization sensitive sensor for such measurements must be considered in depth. It may be necessary to decrease the sensitivity loss in the polarimeter to address range increase by polarization filtering.

VIII FUTURE WORK

The recommended future work for the split-field polarimeter includes the following:

- Measure the modulation transfer function (MTF) of each component in the polarimeter; the collimator optics, the beam splitter polarizer and even the mirrors. This is to single out the component that is causing the degradation in the entire system performance.
- Test the germanium anti-reflection coated aspheric lens. With the degraded coating large reflection losses and scattered radiation may occur.
- The radiation emitted by the gold mirrors is still a problem. To resolve this problem the housings need to be redesigned for a cooling system to bring the entire system internal temperature to say 0°C. This will minimize the emission from the mirrors.
- Develop a computer model of the polarimeter to aid in future analysis of this system. With known transmittance and reflectance of the optical elements, the performance of the polarimeter is predicted and hence the performance is optimized with the right optics.
- Design a test for contrast enhancement by polarized background suppression. Will MRT loss in the polarimeter prevent this being observed?

THIS PAGE IS INTENTIONALLY LEFT BLANK

APPENDIX A

MATLAB CODES

The following Matlab codes are presented in this Appendix:

Planck.m – to generate the Planck blackbody curve for Figure 2.2

Plot_MRTD.m – to generate the MRTD curve for the three configurations as in Figures 6.1, 6.2, 6.3 & 6.4

TTPF.m – to generate the target transfer probability function curve as in Figure 6.8

MRTD_Range.m – to generate the MRTD as a function as range, the Apparent TBTD as a function of range and the merger of the two plots as shown in Figures 6.10, 6.11 & 6.12

```

%      Program Title: Planck.m
%      Program generates the Plank blackbody curve.
%      Figure 2.2

clear
close all
lambda=0:0.01:25;

% Planck's equation for T = 220

T0=220;
C1=3.7418e4;
C2=1.4388e4;
M0=exp(C2./(lambda*T0))-1;
M1=(C1./(lambda.^5));
M220=M1./M0;

%Planck's equation for T=250;

T1=250;
M2=exp(C2./(lambda*T1))-1;
M250=M1./M2;

%Planck's equation for T=280;

T2=280;
M3=exp(C2./(lambda*T2))-1;
M280=M1./M3;

%Planck's equation for T=3000;

T3=300;
M4=exp(C2./(lambda*T3))-1;
M300=M1./M4;

%Planck's equation for T=320;

T4=320;
M5=exp(C2./(lambda*T4))-1;
M320=M1./M5;

```

```

%Wien's Displacement Law

I0=2897/T0;
I1=2897/T1;
I2=2897/T2;
I3=2897/T3;
I4=2897/T4;

L=[I0,I1,I2,I3,I4];
maxima=[max(M220),max(M250),max(M280),max(M300),max(M320)];

%Plots the results
figure(1)
plot(lambda,M250,lambda,M280,lambda,M300,lambda,M320,L,maxima,'-');
grid on;
gtext('250k');
gtext('280k');
gtext('300k');
gtext('320k');
xlabel('Wavelength - (μm)');
ylabel('Spectral Radiant Exitance - M');

```

```

%      Program Title: Plot_MRTD.m
%      Program generates the MRTD curve for the three configurations.
%      Figure 6.1, 6.2, 6.3 & 6.4
%      TI only

data_2 = [1.77, 1.55, 0.44, 0.33, 0.27, 0.22, 0.11]; %1.77
target_2 = [8, 8.5, 9, 10, 12, 14, 18];
distance_2 = 2.0; % 2.0 meters
SF_2 = 4./(target_2 ./ distance_2);
%fit_data1 = [0, 0.03, 0.06, 0.07, 0.10, 0.16, 0.20, 0.28, 0.35, 0.45, 0.75, 1.0, 2.0, 3.5, 4.5, 5.5, 6];
%fit_SF1 = [0, 0.1, 0.2, 0.3, 0.4, 0.5, 0.6, 0.7, 0.8, 0.85, 0.92, 0.94, 0.97, 1.0, 1.015, 1.03, 1.04];

SL = 0.05;
SC = 0.0055;
ER = 2.04;
r = [0:0.05:6];

MRT = SL + SC.*(2.*r./sqrt(7)).*exp((pi./2).*ER^2.*r.^2);
figure (1);
plot(SF_2,data_2,'s');
hold on
plot(r,MRT);
%plot(fit_SF1,fit_data1,'k-');
axis([0 1.2 0 6]);
xlabel('Spatial Frequency (cyc/mrad)');
ylabel('Minimum Resolvable Temperature (C)');
title('MRT against Spatial Frequency Plot');

%      Figure 6.2
%      TI with external polarizer

data_epol = [3.5, 3.11, 0.55, 0.5, 0.38, 0.33, 0.28];
target_2 = [8, 8.5, 9, 10, 12, 14, 18];
distance_2 = 2.0; % 2.0 meters
SF_2 = 4./(target_2 ./ distance_2);
%fit_data = [0, 0.05, 0.1, 0.15, 0.2, 0.25, 0.3, 0.35, 0.45, 0.55, 0.8, 1, 2, 4, 5, 6];
%fit_SF = [0, 0.1, 0.2, 0.3, 0.4, 0.5, 0.6, 0.7, 0.8, 0.85, 0.9, 0.92, 0.95, 0.98, 0.99, 1];
SL = 0.05;
SC = 0.05;
ER = 1.75;
r = [0:0.05:6];

MRT = SL + SC.*(2.*r./sqrt(7)).*exp((pi./2).*ER^2.*r.^2);

```

```

figure (1);
plot(SF_2,data_epol,'s');
hold on
plot(r,MRT);
%plot(fit_SF,fit_data,'k-');
axis([0 1.2 0 6]);
xlabel('Spatial Frequency (cyc/mrad)');
ylabel('Minimum Resolvable Temperature (C)');
title('MRT against Spatial Frequency Plot');

%      Figure 6.3
% TI with polarimeter

data_pol = [5, 4.27, 3.77, 3.0, 2.3, 1.8, 1.38];
target_2 = [8, 8.5, 9, 10, 12, 14, 18];
distance_2 = 2.0; % 2.0 meters
SF_2 = 4./(target_2 ./ distance_2);
%fit_data2 = [0, 0.28, 0.57, 0.90, 1.2, 1.5, 1.9, 2.4, 3.0, 3.7, 3.9, 4.2, 4.6, 6];
%fit_SF2 = [0, 0.1, 0.2, 0.3, 0.4, 0.5, 0.6, 0.7, 0.8, 0.9, 0.92, 0.95, 0.97, 0.99];

SL = 0.05;
SC = 1.89;
ER = 0.93;
r = [0:0.05:6];

MRT = SL + SC.*(2.*r./sqrt(7)).*exp((pi./2).*ER^2.*r.^2);

figure (1);
plot(SF_2,data_pol,'s');
hold on
plot(r,MRT);
%plot(fit_SF2,fit_data2,'k-');
axis([0 1.2 0 6]);
xlabel('Spatial Frequency (cyc/mrad)');
ylabel('Minimum Resolvable Temperature (C)');

title('MRT against Spatial Frequency Plot');

%      Figure 6.4
% Plot the three best fitted curve
% TI only

```

```

SL_TI = 0.05;
SC_TI = 0.0055;
ER_TI = 2.04;
r = [0:0.05:6];
MRT_TI = SL_TI + SC_TI.*(2.*r./sqrt(7)).*exp((pi./2).*ER_TI^2.*r.^2);

% TI with Ext. Pol
SL_EP = 0.05;
SC_EP = 0.05;
ER_EP = 1.75;
r = [0:0.05:6];
MRT_EP = SL_EP + SC_EP.*(2.*r./sqrt(7)).*exp((pi./2).*ER_EP^2.*r.^2);

% TI with Polarimeter
SL_P = 0.05;
SC_P = 1.89;
ER_P = 0.93;
r = [0:0.05:6];

MRT_P = SL_P + SC_P.*(2.*r./sqrt(7)).*exp((pi./2).*ER_P^2.*r.^2);

% Plot the three best fitting curves
figure (4)

plot(r,MRT_TI,'k-');
hold on;
plot(r,MRT_EP,'b-');
plot(r,MRT_P,'r-');
axis([0 1.2 0 6]);
xlabel('Spatial Frequency (cyc/mrad)');
ylabel('Minimum Resolvable Temperature (C)');
title('MRT against Spatial Frequency Plot');
legend('TI only','TI with Polarizer','TI with Polarimeter');

```

```

%      Program Title: TTPF.m
%      Program generates the target transfer probability function curve.
%      Figure 6.8

clear
i = 1;
for n = 0:0.1:2
    e = 2.7 + 0.7*n;
    P(i) = (n^e)/(1+n^e);
    N_N5(i) = (i-1)/10;
    i = i+1;
end
figure(1)
plot(N_N5,P);
xlabel('N/N50');
ylabel('Probability');
title('Target transfer probability function');
axis([0 2 0 1]);
grid on

```

```

%      Program Title: MRTD_Range.m
%      Program generates the MRTD as a function of range curve for the three configurations.
%      Generates the Figure 6.10, 6.11,& 6.12
%      clear all

% TI only
SL_TI = 0.05;
SC_TI = 0.0055;
ER_TI = 2.04;
r = [0:0.05:6];

MRT_TI = SL_TI + SC_TI.*(2.*r./sqrt(7)).*exp((pi./2).*ER_TI^2.*r.^2);

% TI with Ext. Pol
SL_EP = 0.05;
SC_EP = 0.05;
ER_EP = 1.75;
r = [0:0.05:6];

MRT_EP = SL_EP + SC_EP.*(2.*r./sqrt(7)).*exp((pi./2).*ER_EP^2.*r.^2);

% TI with Polarimeter
SL_P = 0.05;
SC_P = 1.89;
ER_P = 0.93;
r = [0:0.05:6];

MRT_P = SL_P + SC_P.*(2.*r./sqrt(7)).*exp((pi./2).*ER_P^2.*r.^2);

% Plot the three best fitting curves
figure (1)
plot(r,MRT_TI,'k-');
hold on;
plot(r,MRT_EP,'b-');
plot(r,MRT_P,'r-');
axis([0 1.2 0 6]);
xlabel('Spatial Frequency (cyc/mrad)');
ylabel('Minimum Resolvable Temperature (C)');
title('MRT against Spatial Frequency Plot');
legend('TI only','TI with Polarizer','TI with Polarimeter');

% Converting the plot MRTD against spatial frequency to MRTD against range

```

```

Dc = 15; % Critical diamension is 15m
N = 2; % Detection

R = (2.* Dc .* r)./N;
%Range_epol = (2.* Dc .* fit_SF)./N;
%Range_pol = (2.* Dc .* fit_SF2)./N;
%MRT_TI_R = SL_TI + SC_TI.*(2.*R./sqrt(7)).*exp((pi./2).*ER_TI^2.*R.^2);
%MRT_EP_R = SL_EP + SC_EP.*(2.*R./sqrt(7)).*exp((pi./2).*ER_EP^2.*R.^2);
%MRT_P_R = SL_P + SC_P.*(2.*R./sqrt(7)).*exp((pi./2).*ER_P^2.*R.^2);

%To calculate the apparent temperature for object delta T of 10 deg
Range = [0,0.1,1,2,3,4,5,6,7,8,9,10,11,12,13,14,15,16];
tau = [1, 0.6379, 0.4132, 0.3218, 0.2649, 0.2243, 0.1932, 0.1686, 0.1485, 0.1318, 0.1178, 0.1058, 0.0955,
0.0865, 0.0787, 0.0718, 0.0657, 0.0602];
Delta_T = 10;
Tapp = Delta_T.*tau;

figure (2)
plot(R,MRT_TI,'k-');
hold on;
plot(R,MRT_EP,'b-');
plot(R,MRT_P,'r-');
axis([0 16 0 6]);
xlabel('Range (km)');
ylabel('Minimum Resolvable Temperature (C)');
ylabel('Apparent Temperature Difference(C)');
title('MRTD and Apparent Temperature Difference against Range');
%legend('TI only','TI with Polarizer','TI with Polarimeter','Apparent Temperature');
legend('TI only','TI with Polarizer','TI with Polarimeter');

% Figure 6.11 & Figure 6.12

clear all

% TI only
SL_TI = 0.05;
SC_TI = 0.0055;
ER_TI = 2.04;
r = [0:0.05:6];

MRT_TI = SL_TI + SC_TI.*(2.*r./sqrt(7)).*exp((pi./2).*ER_TI^2.*r.^2);

% TI with Ext. Pol

```

```

SL_EP = 0.05;
SC_EP = 0.05;
ER_EP = 1.75;
r = [0:0.05:6];

MRT_EP = SL_EP + SC_EP.*(2.*r./sqrt(7)).*exp((pi./2).*ER_EP^2.*r.^2);

% TI with Polarimeter
SL_P = 0.05;
SC_P = 1.89;
ER_P = 0.93;
r = [0:0.05:6];

MRT_P = SL_P + SC_P.*(2.*r./sqrt(7)).*exp((pi./2).*ER_P^2.*r.^2);

% Plot the three best fitting curves
figure (1)
plot(r,MRT_TI,'k-');
hold on;
plot(r,MRT_EP,'b-');
plot(r,MRT_P,'r-');
axis([0 1.2 0 6]);
xlabel('Spatial Frequency (cyc/mrad)');
ylabel('Minimum Resolvable Temperature (C)');
title('MRT against Spatial Frequency Plot');
legend('TI only','TI with Polarizer','TI with Polarimeter');

% Converting the plot MRTD against spatial frequency to MRTD against range

Dc = 15; % Critical dimension is 15m
N = 2; % Detection

R = (2 .* Dc .* r)./N;
%Range_epol = (2 .* Dc .* fit_SF)./N;
%Range_pol = (2 .* Dc .* fit_SF2)./N;
%MRT_TI_R = SL_TI + SC_TI.*(2.*R./sqrt(7)).*exp((pi./2).*ER_TI^2.*R.^2);
%MRT_EP_R = SL_EP + SC_EP.*(2.*R./sqrt(7)).*exp((pi./2).*ER_EP^2.*R.^2);
%MRT_P_R = SL_P + SC_P.*(2.*R./sqrt(7)).*exp((pi./2).*ER_P^2.*R.^2);

%To calculate the apparent temperature for object delta T of 10 deg

```

```

Range = [0,0.1,1,2,3,4,5,6,7,8,9,10,11,12,13,14,15,16];
tau = [1, 0.6379, 0.4132, 0.3218, 0.2649, 0.2243, 0.1932, 0.1686, 0.1485, 0.1318, 0.1178, 0.1058, 0.0955,
0.0865, 0.0787, 0.0718, 0.0657, 0.0602];

Delta_T = 10;
Tapp = Delta_T.*tau;

figure (2)
plot(R,MRT_TI,'k-');
hold on;
plot(R,MRT_EP,'b-');
plot(R,MRT_P,'r-');
plot(Range,Tapp,'g*-')

axis([0 16 0 6]);
xlabel('Range (km)');
ylabel('Minimum Resolvable Temperature (C)');
ylabel('Apparent Temperature Difference(C)');
title('MRTD and Apparent Temperature Difference against Range');
%legend('TI only','TI with Polarizer','TI with Polarimeter','Apparent Temperature');
legend('TI only','TI with Polarizer','TI with Polarimeter');

```

THIS PAGE INTENTIONALLY LEFT BLANK

LIST OF REFERENCES

1. A.W. Cooper, W.J. Lentz, P.L. Walker, P.M. Chan, "Infrared Polarization Measurements of Ship Signatures and Background Contrast", SPIE Proceedings, SPIE International Symposium on Optical Engineering in Aerospace Sensing, Orlando, FL, 1992.
2. A.W. Cooper, W.J. Lentz, P.L. Walker, P.M. Chan, "Polarization Enhancement of Contrast in Infrared Ship/Background Imaging", Paper 26 AGARD SPP Symposium on Propagation Assessment in Coastal Environments 1994, AGARD Proceeding CP576, 1995.
3. D.J. Gregoris, S.Yu, A.W. Cooper, E.A. Milne, "Dual-band Infrared Polarization Measurements of Sun Glint from the Sea Surface", SPIE Proceedings, Vol. 1687, 1992.
4. Heisey, P.H., "Split-Field and Internally Filtered Imaging Polarimeter Development and Testing", Masters Thesis, Naval Postgraduate School, June 1996.
5. Hudson, R., Infrared System Engineering, John Wiley & Sons, 1969.
6. Holst, G. C., Electro-Optical Imaging System Performance, JCD Publishing and SPIE Optical Engineering Press, 2000.
7. Hecht, E., Optics, Addison Wesley, Reading, MA, 1998.
8. Pedrotti, F., Pedrotti, L., Introduction to Optics, Prentice Hall, Inc., 1987
9. Collett, E., Polarized Light: Fundamentals and Applications, Marcel Dekker, Inc., New York, 1993
10. Saunders, P., "Radiance of Sea and Sky in the Infrared Window 800-1200 cm^{-1} ", Journal of the Optical Society of America, Vol 58, No 5, May 1968.
11. D.L. Jordan, G. Lewis, "Infrared Polarization Signatures," AGARD Meeting on Atmospheric Propagation Effects through Natural and Man-made Obscurants for Visible to MM-Wave Radiation", May 1993.
12. M. Sidran, "Broadband Reflectance and Emissivity of Specular and Rough Water Surfaces", Applied Optics, Vol 20, No.18, September 1981.

13. J.R. Maxwell, J.L. Beard, C. Due, "Polarization in the Thermal Infrared" Presented at the workshop on Detection, Discrimination and Classification of Targets in Clutter, November 1990.
14. T.J. Rogne, F.G. Smith, J.E. Rice, "Passive Target Detection Using Polarized Components of Infrared Signatures", SPIE Proceedings on Polarimetry: Radar Infrared, Visible, Ultraviolet and X-ray, Vol. 1317, 1990.
15. Johnson, K. D., "Calibration and Algorithm Development for Split-Field Polarimeter", Masters Thesis, Naval Postgraduate School, September 1999.
16. Wolfe L. W. and Zissis J. G., The Infrared Handbook, Office of Naval Research, Department of Navy, Washington, DC, 1978.
17. James D. Howe, Electro-Optical Imaging System Performance Prediction, The Infrared & Electro-Optical System Handbook Vol 4 Chapter 2, 1993.

INITIAL DISTRIBUTION LIST

1. Defense Technical Information Center
Ft. Belvoir, Virginia
2. Dudley Knox Library
Naval Postgraduate School
Monterey, California
3. Department Chairman, Code PH
Department of Physics
Naval Postgraduate School
Monterey, California
4. Professor A. W. Cooper, Code PH/Cr
Department of Physics
Naval Postgraduate School
Monterey, California
5. Professor Gamani Karunasiri, Code PH/Kg
Department of Physics
Naval Postgraduate School
Monterey, California
6. Director, Temasek Defence System Institute
Prof Yeo Tat Soon
Singapore
7. Defence Science & Technology Agency, Singapore
Tung, Yan Foo
Singapore